



# **Estuary, Lake and Coastal Ocean Model: ELCOM**

## **v2.2 Science Manual**

Ben Hodges and Chris Dallimore.

Contract Research Group  
Centre for Water Research  
University of Western Australia.  
June 15, 2006



# Contents

|  |            |
|--|------------|
| <b>List of Figures</b>                               | <b>v</b>   |
| <b>List of Tables</b>                                | <b>vii</b> |
| <b>1 Introduction</b>                                | <b>1</b>   |
| 1.1 Overview . . . . .                               | 1          |
| <b>2 Governing Hydrodynamic equations and models</b> | <b>3</b>   |
| <b>3 Timestep limitations</b>                        | <b>5</b>   |
| <b>4 Numerical Method</b>                            | <b>7</b>   |
| 4.1 Introduction . . . . .                           | 7          |
| 4.2 Semi-implicit formulation for momentum . . . . . | 7          |
| 4.3 Horizontal diffusion discretization . . . . .    | 9          |
| 4.4 Baroclinic discretization . . . . .              | 9          |
| 4.5 Free surface discretization . . . . .            | 9          |
| 4.6 Advective discretization . . . . .               | 10         |
| 4.6.1 Linear semi-Lagrangian methods. . . . .        | 10         |
| 4.6.2 Linear semi-Lagrangian methods. . . . .        | 11         |
| 4.7 Scalar transport. . . . .                        | 13         |
| 4.7.1 Scalar horizontal diffusion. . . . .           | 16         |
| 4.8 Sidewall and bottom boundary conditions. . . . . | 16         |
| 4.9 Wind momentum model . . . . .                    | 17         |
| <b>5 Surface Thermodynamics and Mass fluxes</b>      | <b>19</b>  |
| 5.1 Introduction . . . . .                           | 19         |
| 5.2 Surface energy fluxes . . . . .                  | 19         |
| 5.2.1 Solar (shortwave) radiation flux . . . . .     | 19         |
| 5.3 Long wave energy flux . . . . .                  | 20         |
| 5.3.1 Incident long wave radiation: . . . . .        | 20         |
| 5.3.2 Nett long wave radiation: . . . . .            | 21         |
| 5.3.3 Cloud cover: . . . . .                         | 21         |
| 5.4 Sensible heat flux . . . . .                     | 22         |
| 5.5 Latent heat flux . . . . .                       | 22         |
| 5.6 Surface mass fluxes . . . . .                    | 22         |

|          |  |           |
|----------|--|-----------|
| 5.6.1    | Latent heat mass flux density . . . . .              | 22        |
| 5.6.2    | Rainfall . . . . .                                   | 23        |
| 5.7      | Atmospheric stability and surface exchange . . . . . | 23        |
| <b>6</b> | <b>Mixing Model</b>                                  | <b>25</b> |
| 6.1      | Introduction . . . . .                               | 25        |
| 6.2      | Energy terms in the mixed layer model . . . . .      | 25        |
| 6.3      | A Mixing timestep . . . . .                          | 27        |
| <b>7</b> | <b>Numerical Diffusion Filter</b>                    | <b>33</b> |
| <b>8</b> | <b>Underflow Model</b>                               | <b>35</b> |
| 8.1      | Introduction . . . . .                               | 35        |
| 8.2      | Governing Equations . . . . .                        | 35        |
| 8.3      | Model Implementation . . . . .                       | 36        |
| 8.4      | Front tracking . . . . .                             | 38        |
| 8.5      | Coupling the model to ELCOM . . . . .                | 39        |
| 8.6      | Plunge Point Analysis . . . . .                      | 42        |
| <b>9</b> | <b>Artificial Destratification</b>                   | <b>45</b> |
| 9.1      | Introduction . . . . .                               | 45        |
| 9.2      | Bubble Plumes . . . . .                              | 45        |
| 9.2.1    | Initialisation: . . . . .                            | 45        |
| 9.2.2    | Subsequent entrainment: . . . . .                    | 47        |
| 9.2.3    | Detrainment: . . . . .                               | 47        |
| 9.3      | Pumps/Jets . . . . .                                 | 48        |
| 9.3.1    | Initialisation: . . . . .                            | 48        |
| 9.3.2    | Subsequent entrainment: . . . . .                    | 48        |
| 9.3.3    | Detrainment: . . . . .                               | 48        |

## List of Figures

|     |                              |    |
|-----|------------------------------|----|
| 4.1 | 2D Euler-Lagrange . . . . .  | 13 |
| 4.2 | 3d Euler-Lagrange . . . . .  | 14 |
| 6.1 | Mixing Layers . . . . .      | 26 |
| 8.1 | Underflow Coupling . . . . . | 40 |
| 9.1 | insertion . . . . .          | 46 |



## List of Tables

|   |   |
|---|---|
| 2.1 Summary of Governing Hydrodynamic equations . . . . . | 4 |
|---|---|



## Introduction

### 1.1 Overview

ELCOM (Estuary, Lake and Coastal Ocean Model) is a three-dimensional hydrodynamics model for lakes and reservoirs, and is used to predict the variation of water temperature and salinity in space and time. The model forms the three-dimensional hydrodynamics driver to the CAEDYM water quality model.

Heat exchange through the water's surface is governed by standard bulk transfer models found in the literature (e.g., Amorocho and Devries (1980); Imberger and Patterson (1981); Jacquet (1983)). The energy transfer across the free surface is separated into nonpenetrative components of long-wave radiation, sensible heat transfer, and evaporative heat loss, complemented by penetrative shortwave radiation. Nonpenetrative effects are introduced as sources of temperature in the surface-mixed layer, whereas penetrative effects are introduced as source terms in one or more grid layers on the basis of an exponential decay and an extinction coefficient (Beer's law).

ELCOM computes a model time step in a staged approach consisting of

1. introduction of surface heating/ cooling in the surface layer
2. mixing of scalar concentrations and momentum using a mixed-layer model
3. introduction of wind energy as a momentum source in the wind-mixed layer
4. solution of the free-surface evolution and velocity field
5. horizontal diffusion of momentum
6. advection of scalars, and
7. horizontal diffusion of scalars

The fundamental numerical scheme is adapted from the TRIM approach of Casulli and Cheng (1992) with modifications for accuracy, scalar conservation, numerical diffusion, and implementation of a mixed-layer turbulence closure. The solution grid uses varying width orthogonal cells. The grid stencil is the Arakawa C-grid: Velocities are defined on cell faces with the free-surface height and scalar concentrations on cell centers. The free-surface height in each column of grid cells moves vertically through grid layers as required by the free-surface evolution equation. Replacement of the standard vertical turbulent diffusion equation with a mixed-layer model eliminates the tridiagonal matrix inversion for each horizontal velocity component and transported scalar required for each grid water column in the original TRIM scheme. This provides computational efficiency and allows sharper gradients to be maintained with coarse grid resolution.



## Governing Hydrodynamic equations and models

The governing equations and fundamental models used for three-dimensional transport and surface thermodynamics in ELCOM are summarized in Table 2.1. The transport equations are the unsteady Reynolds-averaged Navier-Stokes (RANS) and scalar transport equations using the Boussinesq approximation and neglecting the non-hydrostatic pressure terms. The free surface evolution is governed by an evolution equation developed by a vertical integration of the continuity equation applied to the Reynolds-averaged kinematic boundary condition.

The unsteady RANS equations are developed by filtering the unsteady Navier-Stokes equations over a time period that is long relative to sub-grid scale processes, but small relative to the unsteady grid-scale processes that are of interest. In an unsteady RANS numerical method the time scale of the averaging is the time step used in advancement of the evolution equations. Thus, the maximum time step for a given grid resolution is fundamentally limited by the grid scale physics, regardless of the numerical method. This is an important point that is lost when "unconditionally stable" numerical methods are discussed: *the stability of the method at a large time step is irrelevant if the size of the time step implies a temporal averaging scale that encompasses grid-scale motions*. In most numerical approaches, the sub-time scale nonlinear terms  $\overline{u'_i u'_j}$  are represented by an eddy viscosity  $\nu_{jk}$  defined in a tensor form as:

$$\nu_{jk} \frac{\partial u_i}{\partial x_k} = \delta_{jk\nu} \frac{\partial u_i}{\partial x_k} - \overline{u'_i u'_j} \quad (2.10)$$

where  $\delta$  is the molecular viscosity,  $u'_i$  are the sub-time-scale velocity fluctuations, and the overbar indicates the Reynolds-averaging filter. The off-diagonal eddy-viscosity terms are generally set to zero and the molecular viscosity is ignored so that we obtain:

$$\nu_1 \frac{\partial u_i}{\partial x_1} = \overline{u'_i u'_1}; \nu_2 \frac{\partial u_i}{\partial x_2} = \overline{u'_i u'_2}; \nu_3 \frac{\partial u_i}{\partial x_3} = \overline{u'_i u'_3} \quad (2.11)$$

In ELCOM, eddy-viscosity is used to represent the horizontal turbulence closure. In the vertical direction, ELCOM can apply either a vertical eddy viscosity or a mixed-layer model discussed in Chapter 6.

The free-surface evolution is governed by vertical integration of the continuity equation for incompressible flow from the bottom (b) of the water column to the free surface (h) applied to the kinematic boundary condition (e.g. Kowalik and Murty (1993)). To derive the Reynolds-averaged free-surface evolution the Reynolds-averaging filter must be applied to the kinematic boundary condition, resulting in

$$\frac{\partial \eta}{\partial t} = U_3 - U_\alpha \frac{\partial \eta}{\partial x_\alpha} - \frac{\partial}{\partial x_\alpha} (\overline{u'_\alpha h'}) \quad (2.12)$$

Table 2.1 Summary of Governing Hydrodynamic equations used in ELCOM.

---

*Transport of Momentum:*

$$\frac{\partial U_\alpha}{\partial t} + U_j \frac{\partial U_\alpha}{\partial x_j} = -g \left\{ \frac{\partial \eta}{\partial x_\alpha} + \frac{1}{\rho_0} \frac{\partial}{\partial x_\alpha} \int_z^\eta \rho' dz \right\} + \frac{\partial}{\partial x_1} \left\{ \nu_1 \frac{\partial U_\alpha}{\partial x_1} \right\} + \frac{\partial}{\partial x_2} \left\{ \nu_2 \frac{\partial U_\alpha}{\partial x_2} \right\} + \frac{\partial}{\partial x_3} \left\{ \nu_3 \frac{\partial U_\alpha}{\partial x_3} \right\} - \text{pdfilon}_{\alpha\beta} f U_\beta \quad (2.1)$$

*Continuity:*

$$\frac{\partial U_j}{\partial x_j} = 0 \quad (2.2)$$

*Momentum Boundary Conditions - Free Surface:*

$$\frac{\partial U_\alpha}{\partial x_3} = 0 \quad (2.3)$$

*Momentum Boundary Conditions - Bottom and Sides:*

$$U_i = 0 \quad (2.4)$$

*transport of Scalars:*

$$\frac{\partial C}{\partial t} + \frac{\partial}{\partial x_j} (C U_j) = \frac{\partial}{\partial x_1} \left\{ \kappa_1 \frac{\partial C}{\partial x_1} \right\} + \frac{\partial}{\partial x_2} \left\{ \kappa_2 \frac{\partial C}{\partial x_2} \right\} + \frac{\partial}{\partial x_3} \left\{ \kappa_3 \frac{\partial C}{\partial x_3} \right\} + S_c \quad (2.5)$$

*Scalar Boundary Conditions :*

$$\frac{\partial C_\alpha}{\partial x_j} = 0 \quad (2.6)$$

*Free-Surface Evolution:*

$$\frac{\partial \eta}{\partial t} = - \frac{\partial}{\partial x_\alpha} \int_0^\eta u_\alpha dz \quad (2.7)$$

*Free-Surface wind shear:*

$$(u_*)_\alpha^2 = C_{10} \frac{\rho_{air}}{\rho_{water}} (W_\beta W_\beta)^{\frac{1}{2}} W_\alpha \quad (2.8)$$

*Momentum input by wind:*

$$\frac{\partial U_\alpha}{\partial t} = \frac{(U_*)_\alpha^2}{h} \quad (2.9)$$


---

Note that the sub-time scale correlation term  $(\overline{u'_\alpha h'})$  has not been discussed in the literature as the Reynolds-averaging filter has not been rigorously applied to boundary conditions; the equivalent term in large-eddy simulation is discussed in Hodges and Street (1999). The modeling of this term remains an unexplored area of free-surface flows; thus we are forced to assume that it is either small or only of local importance. In the former case it is readily neglected. In the latter case, the present use of implicit discretization of the free-surface solution is numerically diffusive at high barotropic CFL conditions, so local barotropic effects are not well-resolved. Thus, neglecting the subtime-scale nonlinear effects is justified by our focus on basin-scale baroclinic motions. However, we can speculate that the nonlinear correlation  $(\overline{u_\alpha h_\alpha})$  might be both large and non-local where nonlinear sub-basin-scale surface waves enter shallow or restricted waters. The neglect of this term is predicated on the assumption that sub-time scale nonlinear effects do not significantly effect the local mean free-surface height. In general, this is a good assumption for the resolution typically achieved in simulations of lakes and estuaries, and will be used herein. The free surface boundary condition is an approximate form of the dynamic boundary condition that neglects: dynamic pressure, local horizontal variation of the wind, updrafts, downdrafts and surface tension. This is appropriate for lake simulations using the hydrostatic approximation.

## Timestep limitations

Both TRIM and ELCOM are unconditionally stable for purely barotropic flows; that is, they will produce stable numerical results for any size of time step. However, for stratified flows, both methods use explicit discretization of the baroclinic terms in the momentum equation leading to a time step constraint based on the internal wave Courant-Friedrichs-Lewy condition (*CFL*) such that

$$(g'D)^{1/2} \frac{\Delta t}{\Delta x} < \sqrt{2} \quad (3.1)$$

is required. The left-hand side is defined as the baroclinic *CFL* number ( $CFL_b$ ), where  $g'$  is the reduced gravity due to stratification, the effective depth is  $D$ ,  $\sqrt{g'D}$  is an approximation of the wave speed of an internal wave. This baroclinic stability condition is generally the most restrictive condition in a density-stratified flow. The importance of the internal wave speed can be seen in a simple scaling analysis: Typical lake stratifications provide a modified gravity of  $g' \sim O(10^{-2})ms^{-2}$  while lake depths  $D$  are  $O(10)m$  to  $O(10^2)m$ . Internal waves propagate at  $C \sim \sqrt{g'D}$ , giving wave speeds of  $O(1)ms^{-1}$ . Maximum horizontal water velocities in a lake are typically  $O(10^{-1})ms^{-1}$ , and the desired horizontal grid size is  $O(10^2)m$ .

The maximum allowable time step for a limiting *CFL* condition is:

$$\Delta t < \frac{CFL\Delta x}{U} \quad (3.2)$$

If  $U$  is taken as the horizontal water velocity, the maximum allowable time step for a limiting *CFL* of one is  $O(10^3)s$ . If  $U$  is taken as the internal wave speed, the maximum allowable time step for a limiting *CFL* of one is  $O(10^2)s$ . Thus, in the horizontal direction, the internal wave speed rather than the flow velocity controls the maximum allowable time step and high *CFL* capability in the horizontal direction is generally unnecessary. However, in the vertical direction, there is a definite advantage to a numerical scheme that is stable for  $CFL > 1$ . Practical vertical grid resolutions are typically  $O(10^{-1})m$  to  $O(10)m$  depending on the lake morphology and available computational power. Internal wave motions can produce vertical velocities of  $O(10^{-2})ms^{-1}$ , so fine grid resolutions with a *CFL* limit of one can result in an unacceptable time step limitations of  $O(10)s$ .

Scalar transport in ELCOM uses an explicit approach has an advective Courant-Friedrichs-Lewy condition ( $CFL_a$ ) such that  $u \frac{\Delta t}{\Delta x} < 1$  is required. This condition does not effect the time step of the momentum solution ( $\Delta t$ ), but instead is used to compute sub-time s.pdf ( $\Delta t$ ) for the scalar transport solution. The implicit scheme of Gross et al. (1998) does not have *CFL* limitation for vertical velocity and is therefore preferable where fine grid resolution is used in the vertical direction and high vertical *CFL* values are expected. At coarse vertical grid resolutions (low vertical *CFL* values) the present explicit approach should prove more computationally efficient.

A final stability constraint for semi-implicit schemes with explicit horizontal diffusion (e.g. TRIM and ELCOM) is the viscous stability condition (derived for homogenous flows in Casulli and Cheng (1992))

$$\Delta t \leq \frac{\Delta x^2 \Delta y^2}{2\nu(\Delta x^2 + \Delta y^2)} \quad (3.3)$$

This is typically at least an order of magnitude less restrictive than the baroclinic stability condition.

A constraint that becomes important when using large time s.pdf in a geophysical model is whether the velocity field can be considered Lipschitz at the grid and time scales applied: i.e. is the field sufficiently smooth for a numerical approximation (Iserles, 1996). In Smolarkiewicz and Pudykiewicz (1992) the numerical Lipschitz constant  $B$  is defined with the condition that it must be less than unity:

$$B = \left\| \frac{\partial v}{\partial x} \right\| \Delta t < 1 \quad (3.4)$$

This was demonstrated to be a necessary condition in a multi-time-level semi-Lagrangian method to prevent trajectories from intersecting as they are traced back in time and space. While the present Euler-Lagrange method tracks trajectories back only in space, the above Lipschitz condition heuristically applies as a fundamental statement of the necessary behavior of the velocity field to allow reasonable approximation by a numerical model. As demonstrated in Smolarkiewicz and Pudykiewicz (1992), a numerical method may remain stable at a high  $B$ , but the results will not be accurate. This places a fundamental limit on the allowable time step that may be reasonably used in a model. The importance of this point is that the maximum time step that can be used may be a function of the physics, rather than the stability of the numerical method.

## Numerical Method

### 4.1 Introduction

The governing equations are discretized on a Cartesian solution grid in a staggered formulation where single velocity components are defined on each face and scalars are defined at the cell centers. In discrete equations, the cell faces are represented by subscripts such as  $i + 1/2$ , while the centers are represented with integer  $(i, j, k)$  values. The notation of Casulli and Cheng (1992) is used in the following description. For the discrete form of equations, we will use subscripts to represent the position in discrete  $(i, j, k)$  space. Let  $U_{i,j}^{n+1}$  represent the water column vector of time  $n + 1$  velocity values at position  $(i, j)$ , that exist in the time  $n^*$  solution space for all  $k$  that satisfy

$$b_{i,j} \leq \left| \sum_{m=1}^{k_{max}} \Delta z_{i,j,m}^n \right| \leq \eta_{i,j} \quad (4.1)$$

where  $b_{i,j}$  is the height of the bottom of the domain at point  $(i, j)$ ,  $\eta_{i,j}$  is the height of the free surface, and  $k_{max}$  is the maximum number of grid cells in the vertical direction. Similar definitions are applied for other vector quantities in this manual.

### 4.2 Semi-implicit formulation for momentum

The fundamental semi-implicit evolution of the velocity field can be discretized on the  $n^*$  solution space in a manner similar to the TRIM approach as:

$$U_{i+1/2,j}^{n+1} = A_{i+1/2,j}^n G_{i+1/2,j}^n - g \frac{\delta t}{\delta x} [\theta_1 (\eta_{i+1,j}^{n+1} - \eta_{i,j}^{n+1}) + (1 - \theta_1) (\eta_{i,j}^{n+1} - \eta_{i+1,j}^{n+1})] \quad (4.2)$$

$$V_{i,j+1/2}^{n+1} = A_{i,j+1/2}^n G_{i,j+1/2}^n - g \frac{\delta t}{\delta y} [\theta_1 (\eta_{i,j+1}^{n+1} - \eta_{i,j}^{n+1}) + (1 - \theta_1) (\eta_{i,j}^{n+1} - \eta_{i,j+1}^{n+1})] \quad (4.3)$$

where  $G$  is an explicit source term vector,  $\theta_1$  is the "implicitness" of the free surface (The generalized implicitness option for  $0.5 < \theta_1 < 1.0$  is not coded in ELCOM version 2). The default semi-implicit scheme in ELCOM is a backwards-Euler discretization (i.e.  $\theta_1 = 1$ ) of the free surface evolution that is formally 1st order accurate in time.

It has been demonstrated (Casulli and Cattani, 1994) that the backwards Euler method for solution of the hydrostatic momentum equations can be extended to the general two-level scheme of 4.2 and 4.3 that is formally second-order accurate (when  $\theta_1 = 1$ ). However, in coarse grid modeling, this increase in numerical accuracy does not always result in an increase in model skill. In general, many lake and estuary simulations are conducted where the barotropic mode will be solved with CFL conditions that may range from 5 to 10 or greater. Under these conditions, semi-implicit discretizations may be stable, but the "fidelity" of the representation of the flow physics is a function of the type of flow under consideration. The character of the truncation error is critical to understanding the performance of the method. With the 1st order method, the lead error term is 2nd order and results in damping of waves on the free surface. With the 2nd order method, the leading error term is dispersive and results

in numerical waves on the free surface which propagate across the domain; typically causing a linear barotropic wave to evolve into a steep-fronted bore, causing high velocities in localized areas as the surface wave is affected by topography. Thus, the first order method results in good representation of the shape of the free surface and the local barotropic velocities, but shows excessive damping of the inertial response of the free surface. In contrast, the second order method maintains the energy in the surface wave form with minimal numerical dissipation, but has a poor representation of the wave form. In a hydrostatic solution, the dispersive waves cause spurious local forcing of throughout the water column and are detrimental to the skill of the solution. In contrast, the excessive damping of the surface wave causes a decrease in the large scale motions associated with the barotropic response when the wind relaxes, i.e. the "ringing" of the barotropic mode is damped. In general, a strongly forced system is better modeled with the backwards Euler scheme as the wave energy beyond two or three periods is often irrelevant to the first-order physics.

Using any two-level implicit discretization (Casulli and Cheng, 1992), or any explicit discretization technique, the  $A$  matrix can be represented as:

$$A = \begin{bmatrix} b_n + \gamma_k & c_n & 0 & 0 & 0 \\ a_{n-1} & b_{n-1} & c_{n-1} & 0 & 0 \\ 0 & a_{n-2} & b_{n-2} & c_{n-2} & 0 \\ \vdots & \vdots & \vdots & \vdots & \vdots \\ 0 & 0 & a_2 & b_2 & c_2 \\ 0 & 0 & 0 & a_1 & b_1 + \gamma_1 \end{bmatrix} \quad (4.4)$$

The  $\gamma$  terms in  $A$  are set by boundary conditions, while the  $a$ ,  $b$  and  $c$  terms are:

$$b_k = -a_k + \Delta z_k - c_k \quad (4.5)$$

$$b_k = -\theta_2 \left. \frac{\nu_3 \Delta t}{\Delta z} \right|_{k+1/2} \quad (4.6)$$

$$c_k = -\theta_2 \left. \frac{\nu_3 \Delta t}{\Delta z} \right|_{k-1/2} \quad (4.7)$$

The  $\theta_2$  coefficient is determined by the choice of numerical discretization techniques. For  $\theta_2 = 1$  the vertical viscous term is discretized using a backwards Euler technique. For the mixed-layer model used in ELCOM  $\theta_2 = 0$  and the discretization is explicit with  $A$  is zero for all terms off the main diagonal.

The source terms  $G$  in Equations 4.2 and 4.3 can be represented as:

$$G_{i+1,j/2} = L(\tilde{U}_{i+1,j/2}) - \Delta t \left\{ B_{i+1,j/2}^n + D_x(\tilde{U})_{i+1,j/2} + D_y(\tilde{U})_{i+1,j/2} - f\tilde{V}_{i+1,j/2} \right\} \quad (4.8)$$

$$G_{i,j+1/2} = L(\tilde{V}_{i,j+1/2}) - \Delta t \left\{ B_{i,j+1/2}^n + D_x(\tilde{V})_{i,j+1/2} + D_y(\tilde{V})_{i,j+1/2} - f\tilde{U}_{i,j+1/2} \right\} \quad (4.9)$$

The  $L()$  operator represents advective discretization,  $B()$  represents baroclinic discretization,  $D()$  represents horizontal turbulent diffusion discretization. In ELCOM vertical diffusion is computed using a vertical mixing model. The mixing model is represented as an operator such that:

$$\tilde{U}_{i,j,k} = M(U_{i,j,k}^n) \quad (4.10)$$

The mixing operator  $M()$  is described in detail in Chapter 6.

### 4.3 Horizontal diffusion discretization

While the original TRIM approach (Casulli and Cheng, 1992) applied the discretization of the horizontal diffusive terms at the pathline origin, the additional complexity was not found to provide any significant advantage in the accuracy of the present method. Therefore, the horizontal diffusion terms ( $D_x, D_y$ ) from Equations 4.8 and 4.9 are discretized using a second-order stencil such that

$$D_x(\phi_{i,j,k}^n) = \frac{\nu}{\Delta x^2} (\phi_{i+1,j,k}^n - 2\phi_{i,j,k}^n + \phi_{i-1,j,k}^n) \quad (4.11)$$

### 4.4 Baroclinic discretization

The baroclinic term  $B$  in the  $x$  direction is discretized as:

$$B_{i+1/2,j,k}^n = \frac{g}{\rho_0 \Delta x} \left\{ \sum_{m=k}^F \rho'_{i+1,j,m} - \sum_{m=k}^F \rho'_{i,j,m} \right\} \quad (4.12)$$

f

where  $k = F$  is the cell containing the free surface. Similar expressions for diffusion and baroclinic terms are obtained for the  $y$  direction. The elimination of the vertical diffusion terms in the transport of momentum and scalars equations allows the present scheme to dispense with the tridiagonal matrix inversion for each horizontal velocity component and transported scalar required for each  $(i, j)$  water column in the TRIM scheme.

### 4.5 Free surface discretization

The free surface evolution equation can be discretized as:

$$\eta_{i,j}^{n+1} = \eta_{i,j}^n - \theta_1 \left[ \frac{\Delta t}{\Delta x} \delta_x \{(\Delta Z^n)^T U^{n+1}\} - \frac{\Delta t}{\Delta y} \delta_y \{(\Delta Z^n)^T V^{n+1}\} \right] - (1 - \theta_1) \left[ \frac{\Delta t}{\Delta x} \delta_x \{(\Delta Z^n)^T U^n\} - \frac{\Delta t}{\Delta y} \delta_y \{(\Delta Z^n)^T V^n\} \right] \quad (4.13)$$

where  $\Delta Z$  is a vector of the vertical grid spacing, and the operators  $\delta_x$  and  $\delta_y$  indicate discrete differences, e.g.

$$\delta_x(\phi) = \phi_{i+1/2} - \phi_{i-1/2} \quad (4.14)$$

Substitution of Equations 4.2 and 4.3 into 4.13 provides a pentadiagonal system of equations for the time  $n + 1$  free surface height that is readily solved using a conjugate gradient method. The approach adopted for conjugate gradient solution in ELCOM is similar to TRIM, as detailed in Casulli and Cheng (1992).

#### 4.6 Advective discretization

One of the difficulties of numerical modelling at geophysical scales is the wide range of flow conditions that may be present. In particular, internal waves may intermittently produce strong vertical motions over relatively small regions. Where resolution of internal waves is deemed important, the choice of numerical method is driven by the need for accuracy and stability in a small portion of the overall flow field. While many explicit spatial discretization methods are stable for  $CFL < O(1)$ , their accuracy in 3D computations for  $CFL > O(0.5)$  is generally poor when the flow direction is not aligned with the grid.

The drawback of the quadratic method is that it is computationally expensive. However, for low  $CFL$  regions ( $CFL < 0.1$ ), the solution of a quadratic semi-Lagrangian method is dominated by terms in the same seven-point upwind stencil that is obtained by using quadratic upwind discretization. This similarity can be exploited to reduce the computational requirement in regions of low  $CFL$  without significantly reducing the accuracy of the overall solution method. The concept of applying different schemes in different regions can be generalized into the concept of a "hybrid" numerical method. A general hybrid method is one where different solution schemes are applied in different flow regions based upon a criteria measured in the flow field. For our purposes, the criteria is the  $CFL$ , and we apply one discretization technique for low  $CFL$ , and a different technique for high  $CFL$ .

The present hybrid method has been tested to two levels, using quadratic semi-Lagrangian discretization for regions where ( $0 < CFL < 2$ ). The upper limit cutoff is the maximum CFL that can be computed using a quadratic SL method without requiring the additional computational expense of adjusting the stencil region. As a practical matter, the accuracy of computations for  $CFL > 2$  is questionable, so the upper limit is not an unreasonable requirement. For regions with  $CFL > 2$ , the method applies linear semi-Lagrangian discretization (i.e. the approach used in TRIM) to minimize the computational effort of repositioning the stencil.

**4.6.1 Linear semi-Lagrangian methods.** For a stratified flow, semi-Lagrangian methods are desirable in that they are both accurate and stable in the regime where  $0.1 < CFL < 1$ . As a further advantage, they retain their stability in higher CFL regimes, although their accuracy suffers at high  $CFL$  values unless the flow streamlines are well resolved by the grid. However, in stratified flows, the ability to provide stable solutions for  $CFL > 1$  in the horizontal direction is of secondary importance in the selection of a numerical method. The maximum time step is generally limited by either by (1) the baroclinic wave propagation speed in the region of strongest stratification, or (2) the maximum acceptable numerical diffusion in scalar transport. The former requires wave  $CFL < 1$  for stability, while the latter limitation is a matter of grid resolution and the length of time over which model results

are required.

The semi-Lagrangian form of advection is obtained by finding the approximate point in continuous space (the "Lagrange" point) which would be advected to a discrete point  $(i, j, k)$  by the velocity field  $(U, V, W)$  over the time step  $\Delta t$ . That is, the particle position  $(i, j, k)$  is numerically marched back along the streamlines represented by the velocity field  $U, V, W$ . The  $U, V, W$  field may be obtained from single or multiple time levels, depending upon the accuracy and computational complexity desired. A detailed review of semi-Lagrangian techniques is found in Staniforth and Cote (1991). In a linear, single-time level semi-Lagrangian method, the Lagrange point is found using

$$\delta_x = -U\Delta t \quad (4.15)$$

$$\delta_y = -V\Delta t \quad (4.16)$$

$$\delta_z = -W\Delta t \quad (4.17)$$

The value of a variable  $\phi$  at the Lagrange point is found using a trilinear upwind interpolation:

$$\begin{aligned} \phi_L = & \frac{\delta_x}{\Delta x} \frac{\delta_y}{\Delta y} \frac{\delta_z}{\Delta z} \phi_{i-1, j-1, k-1} \\ & + \left(1 - \frac{\delta_x}{\Delta x}\right) \frac{\delta_y}{\Delta y} \frac{\delta_z}{\Delta z} \phi_{i, j-1, k-1} \\ & + \frac{\delta_x}{\Delta x} \left(1 - \frac{\delta_y}{\Delta y}\right) \frac{\delta_z}{\Delta z} \phi_{i-1, j, k-1} \\ & + \frac{\delta_x}{\Delta x} \frac{\delta_y}{\Delta y} \left(1 - \frac{\delta_z}{\Delta z}\right) \phi_{i-1, j-1, k} \\ & + \frac{\delta_x}{\Delta x} \left(1 - \frac{\delta_y}{\Delta y}\right) \left(1 - \frac{\delta_z}{\Delta z}\right) \phi_{i-1, j, k} \\ & + \left(1 - \frac{\delta_x}{\Delta x}\right) \frac{\delta_y}{\Delta y} \left(1 - \frac{\delta_z}{\Delta z}\right) \phi_{i, j-1, k} \\ & + \left(1 - \frac{\delta_x}{\Delta x}\right) \left(1 - \frac{\delta_y}{\Delta y}\right) \frac{\delta_z}{\Delta z} \phi_{i, j, k-1} \\ & + \left(1 - \frac{\delta_x}{\Delta x}\right) \left(1 - \frac{\delta_y}{\Delta y}\right) \left(1 - \frac{\delta_z}{\Delta z}\right) \phi_{i, j, k} \end{aligned} \quad (4.18)$$

The above constitutes an eight-point stencil for a semi-Lagrangian methods with linear interpolation. As the flow field approaches a uniform 1D flow, the linear semi-Lagrangian technique reduces to a linear upwind method for  $CFL < 1$ . Indeed, it is perhaps easier to think of the semi-Lagrangian method as a 3D linear upwind stencil that is successively repositioned for high  $CFL$  conditions. It follows that linear semi-Lagrange method exhibits the unacceptable levels of numerical diffusion that are characteristic of linear upwind methods. This can be ameliorated by using a quadratic method for interpolation of values at the Lagrange point

**4.6.2 Linear semi-Lagrangian methods.** The quadratic semi-Lagrange method extends the 8-point upwind stencil with trilinear interpolation (used in TRIM) to a 27-point upwind stencil using quadratic Lagrange polynomial interpolation. In the notation of in Casulli and Cheng (1992), the operator interpolates the velocity field (on the x face) to the position  $(i + 1/2 - a, j - b, k - d)$ , where  $a, b$  and  $d$  are real numbers that represent displacements from the  $(i + 1/2, j, k)$  position. This is an estimate of the origination of the pathline of a particle moving through the time n velocity field that ends at the position  $(i + 1/2, j, k)$  after time  $\Delta t$ . A similar notation

is used for the  $y$  faces at  $j + 1/2$ . It is convenient to denote the pathline origination point by a superscript (p) so that the advective operators  $L()$  in Equations 4.2 and 4.3:

$$L(\tilde{U}_{i+1/2,j,k}) = \tilde{U}_{i+1/2-a,j-b,k-d} = \tilde{U}^{(p)} \quad (4.19)$$

The process of computing the pathline origin in 2D for bilinear interpolation is discussed in Casulli and Cheng (1992) and is illustrated in Figure 4.1 for 2D quadratic Lagrange interpolation. For Lagrange interpolation on non-uniform grids it is convenient to consider the physical space coordinates  $(x, y, z)$  that correspond to the  $(i,j,k)$  computational indices. Three-dimensional quadratic Lagrange interpolation to find the value of  $U^{(p)}$  at any point  $(x(p)^{(p)}, y(p)^{(p)}, z(p)^{(p)})$  is computed in three sw.pdf illustrated in Figure 4.2 requiring 9 vertical interpolations of the form

$$\hat{U}_{i+\gamma,j+\zeta} = l_{i+\gamma,j+\zeta}^0 U_{i+\gamma,j+\zeta,k} + l_{i+\gamma,j+\zeta}^1 U_{i+\gamma,j+\zeta,k\pm 1} + U_{i+\gamma,j+\zeta,k} + l_{i+\gamma,j+\zeta}^2 U_{i+\gamma,j+\zeta,k\pm 2} \quad (4.20)$$

where the  $(i, j)$  subscripts denote the position of the vertical line to be interpolated, while  $\gamma$  and  $\zeta$  are  $\pm\{0, 1, 2\}$ , with the sign determined by the upwind direction of the stencil (as is the sign for the  $k$  increment in the  $U$  position subscripts). The Lagrange polynomial coefficients for each  $(i, j)$  line are computed from the standard Lagrange coefficient formula (eg: Al-Khafaji and Tooley (1986))

$$l^m = \prod_{\substack{\zeta = 0 \\ \zeta \neq m}}^2 \frac{z^{(p)} - z_{k\pm\zeta}}{k \pm m - z_{k\pm\zeta}} \quad (4.21)$$

where  $z^p$  is the vertical coordinate of the interpolated point and the sign is determined to obtain an upwind stencil. The vertical interpolations are followed by 3 horizontal interpolations in the  $y$  direction of the form

$$\bar{U}_{i+\gamma} = l_{i+\gamma,j}^0 \hat{U}_{i+\gamma,j} + l_{i+\gamma,j\pm 1}^1 \hat{U}_{i+\gamma,j\pm 1} + l_{i+\gamma,j\pm 2}^2 \hat{U}_{i+\gamma,j\pm 2} \quad (4.22)$$

Finally, a single interpolation in the  $x$  direction is applied as

$$U^{(p)} = l^0 \bar{U}_i + l^1 \bar{U}_{i\pm 1} + l^2 \bar{U}_{i\pm 2} \quad (4.23)$$

The Lagrange coefficients in Equations 4.22 and 4.23 are computed using Equation 4.21 with  $y$  or  $x$  substituted for  $z$  as appropriate. The quadratic stencil used for the Euler-Lagrange interpolation is advantageous as it reduces artificial damping of internal waves that occurs with an 8-node linear stencil; thus improving the ability of the method to resolve the free motions of a stratified basin. While this improvement is necessary for modeling stratified lakes, it is probably of lesser importance in estuarine modeling where forced motions dominate the flow physics.

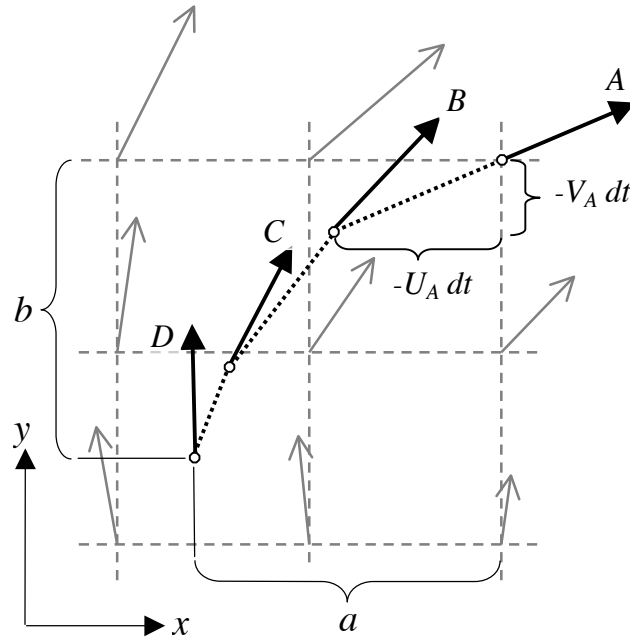


Figure 4.1 Two-dimensional illustration of Euler-Lagrange streamline computation using quadratic Lagrange interpolation. Velocity vector  $A$ , with components  $U_A$  and  $V_A$ , is used to track particle path from position  $(i, j)$  back to the base of vector  $B$  using the momentum sub-time step  $dt$ . Velocity vector  $B$  is computed from the nine grid nodes upwind of the velocity vector at position  $(i, j)$ . Vector  $B$  is used to track the particle path back to the base of velocity vector  $C$ , which is again interpolated from the surrounding nine grid nodes. This is repeated  $n$  times where  $ndt = \Delta t$ . If a vector base position is not contained within the nine upwind grid nodes, the upwind stencil must be repositioned. In the present code, linear interpolation is used for the rare instances when repositioning is necessary. The final vector is the result of the Euler-Lagrange operator in Equations 4.8 and 4.8, i.e.  $L(U_{i,j}), =, U_{(i-a,j-b)}$ . The number of sub-time s.pdf ( $n$ ) may be set arbitrarily, with high values providing greater accuracy and higher computational cost. Note that  $n = 1$  everywhere corresponds to quadratic upwind discretization and has poor accuracy characteristics unless the  $CFL_a \ll 1$ . As a general rule, the minimum  $n$  is set as a local function of the grid and flow field such that  $U \frac{dt}{\Delta x} < 1$

The extra computational requirements of the quadratic stencil are somewhat ameliorated by the ability to compute source terms for flows in the range  $1 < CFL < 2$  without repositioning the stencil.

#### 4.7 Scalar transport.

Scalar transport is (arguably) the most critical piece of the hydrodynamic numerical algorithm for strongly stratified flows. If the scalar transport is not sufficiently accurate, we cannot obtain correct evolution of the density field and internal wave motions. In ELCOM, a conservative third-order scalar transport method is applied. Use of conservative methods has been found critical to stratified lake and estuary models as the distribution of density feeds back into the momentum equation through the baroclinic term. Non-conservation results in loss of momentum in baroclinic forcing such that internal waves are dissipated too rapidly and strong gradients that drive underflows may simply cease to exist. Using non-conservative methods, loss of mass and deterioration of sharp gradients at salinity and temperature fronts degrades the skill of the model.

A three-stage numerical algorithm for transport of a scalar concentration  $C$  can be defined as:



$$\tilde{C} = M(C^n) + S^{(C)} \quad (4.24)$$

$$C^* = \tilde{C} - \Delta t \frac{\partial}{\partial x_j} (\tilde{C} U_j) \quad (4.25)$$

$$\tilde{C} = M(C^n) + S^{(C)} C^{n+1} = C^* - \Delta t \frac{\partial}{\partial x_\alpha} \left( \kappa \frac{\partial C^*}{\partial x_\alpha} \right) + O(\Delta t)^2 \quad (4.26)$$

As with the momentum mixing and source terms, the mixing operator in Equation 4.24 represents vertical mixing by the Reynolds stress term and is discussed in detail in a subsequent section on the vertical mixing model. The  $S^{(c)}$  in Equation 4.24 represents scalar sources (e.g. heat transfer across the free surface into the wind-mixed layer). Equation 4.25 is advection of the scalar field by the resolved flow field, and Equation 4.26 is horizontal diffusion by turbulent motions. For clarity in the above and the following, advection, i.e. Equation 4.25, is defined over time step  $\Delta t$ . However, when  $MAX(CFL_a) > 1$ , the sub-time step  $\delta t$  is used, where  $m\delta t = \Delta t$  and Equation 4.25 is iterated  $m$  times. In the following derivations, substitution of  $\delta t$  for  $\Delta t$  and  $n + m\Delta t$  for  $n + 1$  makes the equations reflect the sub-time step iteration process.

In differential notation, a conservative form of the transport equation is:

$$\tilde{C} = M(C^n) + S^{(C)} \frac{\partial}{\partial t} \int_{\Omega} C d\Omega + \int_{A_x} CU dA_x + \int_{A_y} CU dA_y + \int_{A_z} CU dA_z = S^{(c)} \quad (4.27)$$

where  $\Omega$  is a control volume  $A_x, A_y, A_z$  are surface areas of the control volume faces. For clarity in the discrete form, it will be useful to omit the  $(i, j, k)$  subscript notation for any centered variable so that  $C_{i,j,k}$  is written simply as  $C$ , and  $C_{i,j+1/2,k}$  is written as  $C_{j+1/2}$ . The discrete advected scalar concentration field ( $C^*$ ) written as a flux-conservative advection over the  $n^*$  set of cells is:

$$C^* = \tilde{C} \frac{\Delta Z^n}{\Delta Z^{n+1}} - \frac{\Delta t}{\Delta X \Delta Y \Delta Z^{n+1}} \{ \delta_x Q + \delta_y Q + \delta_z Q \} \quad (4.28)$$

where operators of the form  $\delta_x$  are defined in Equation 4.15.  $Q$  is the scalar flux through the cell faces, defined on the  $n^*$  cell set for the  $i+1/2$  face as:

$$Q_{i+1/2} = \left( \Delta y \Delta Z^{n+1} U^{n+1/2} \tilde{C} \right)_{i+1/2} \quad (4.29)$$

Similar definitions apply on the  $j + 1/2$  and  $k + 1/2$  faces. There is no flux through the uppermost face of cell containing the free surface, so  $Q_{i,j,F+1/2} = 0$ , where  $k = F$  is the cell containing the free surface. It follows that  $\Delta Z_{i,j,F}^{n+1} - \Delta Z_{i,j,F}^n = \Delta t W_{i,j,F+1/2}^{n+1}$  and  $C_{i,j,F+1/2} = C_{i,j,F}$ . For any cell  $(i, j, F)$  in the  $n^*$  set:

$$C_{i,j,F+1/2} = C_{i,j,F} = \frac{\Delta t}{\Delta z^{n+1}} \delta_z (W_{i,j,F+1/2}^{n+1} C_{i,j,F+1/2}) \quad (4.30)$$

Thus, for all cells in the  $n^*$  set (including free surface cells):

$$C^* = \tilde{C} - \frac{\Delta t}{\Delta x} \delta_x(U^{n+1} \tilde{C}) - \frac{\Delta t}{\Delta y} \delta_y(V^{n+1} \tilde{C}) - \frac{\Delta t}{\Delta z^{n+1}} \delta_z(W^{n+1} \tilde{C}) \quad (4.31)$$

Since the scalar concentrations are updated at the cell centers, it is necessary to define a method of interpolation for cell face values such as  $\delta_x(UC)$ . The ULTIMATE flux-limiting filter applied with third-order QUICKEST interpolation (Leonard, 1991) performs particularly well in maintaining monotonic scalar fields while limiting numerical diffusion. Implementation in 2D and demonstration of its effectiveness estuarine flows has been documented by Lin and Falconer (1997). The conservative ULTIMATE QUICKEST method is limited to  $CFL_a < 1$  in all coordinate directions. The present semi-implicit scheme remains stable at higher CFL (providing  $CFL_b$  does not exceed unity), so the ULTIMATE QUICKEST algorithm must be computed successively over sub-time s.pdf such that the maximum  $CFL_a$  is less than one in each sub-time step. In practice, coarse resolution models of strongly stratified basins will have the defining time step limitation based on the baroclinic mode in the momentum solution and  $CFL_a > 1$  may never occur.

The recent evaluation of transport schemes by Gross et al. (1998) did not directly examine the ULTIMATE limiter applied to a QUICKEST approach; however, their results did show that effective results for a 2D model of South San Francisco Bay could be obtained with either the QUICKEST approach or Roe's superbee limiter applied to a Lax-Wendroff method. As Lax-Wendroff is a second-order discretization, it is likely that the ULTIMATE limiter applied to third-order QUICKEST would have been at least as effective as the schemes they tested. The present use of an explicit discretization approach contrasts with the vertical-implicit approach taken in the recent adaptation of TRIM by Gross et al. (1998). The advantage of the latter is that it is stable for scalar transport solutions at  $CFL > 1$ , whereas the present method requires sub-time step iterations of the scalar transport routines when high CFL's are encountered. Thus the approach of by Gross et al. (1998) is preferable for a fine vertical grid resolution while the present method should prove more computationally efficient at coarse grid resolution.

**4.7.1 Scalar horizontal diffusion.** The horizontal diffusion terms in Equation 2.5 are discretized to obtain the time ' $n + 1$ ' scalar field over the solution space ' $n^*$ ':

$$C_{i,j,k}^n = \tilde{C}_{i,j,k} + D_x(\tilde{C}_{i,j,k}) + D_y(\tilde{C}_{i,j,k}) \quad (4.32)$$

where  $D_x$  and  $D_y$  are finite-difference operators for the second derivative. As with the velocity solution, any time  $n + 1$  locations that are not in the time  $n^*$  solution space are updated using the concentration of neighbour cells.

#### 4.8 Sidewall and bottom boundary conditions.

The momentum introduced into a lake by wind forcing is dissipated in the boundary layers of the lake and turbulent processes in the interior. In 2D depth-averaged models the Chezy-Manning bottom stress formulation

has been applied to account for the dissipation in the entire water column. This is particularly useful in providing a method of calibrating depth-averaged coastal/estuarine models to reproduce a given set of tidal data. In a 3D model with stratification, detailed field data for calibrating a bottom friction coefficient is generally not available. Furthermore, without the transfer of basin-scale internal-wave energy to subgrid-scales waves, it is questionable as to whether any boundary condition model in the literature can capture actual boundary dynamics and predict the correct location and timing of dissipation and vertical fluxes. Sidewall boundary conditions (i.e. vertical solid boundaries) are often modeled as free-slip to effect simpler implementation in a numerical method (Casulli and Cheng, 1992). However, the lack of sidewall drag prevents vertical vorticity from being produced at boundaries. As lakes typically have regions of steep slopes and longshore currents (due to Kelvin waves), the neglect of sidewall drag may not be a suitable simplification in modeling basin-scale motions.

There remains much work to be done in developing appropriate bottom and sidewall boundary conditions in coarse grid models. ELCOM provides three basic forms of boundary conditions: (1) no-slip, (2) free-slip, and (3) specified stress.

#### 4.9 Wind momentum model

The momentum input of the wind is typically modeled (e. g., Casulli and Cheng (1992)) using a stress boundary condition at the free surface:

$$\nu \left. \frac{\partial u}{\partial x} \right|_{z=\eta} = u_*^2 \quad (4.33)$$

where  $\nu$  is an eddy viscosity and  $u_*^2$  is the wind stress. This boundary condition requires solution of vertical viscosity/ diffusion terms of the form

$$\frac{\partial}{\partial x} \left\{ \nu \frac{\partial U_\alpha}{\partial x_3} \right\}; \frac{\partial}{\partial x} \left\{ \kappa \frac{\partial C}{\partial x_3} \right\} \quad (4.34)$$

in place of the Reynolds stress terms in the momentum and scalar transport equations, terms that are modeled in ELCOM using the 3D mixed-layer model. As demonstrated by Glorioso and Davies (1995), the formulation chosen for eddy viscosity has a dramatic influence on the development of pressure-driven upwind flows in a wind-forced homogenous system. Using an eddy-viscosity/ diffusivity approach in a stratified system, the depth, downwind velocity, and velocity shear in the wind-mixed layer are functions of the values used for eddy viscosity and diffusivity above the thermocline. The resulting prediction of mixed-layer depth using a coarse vertical grid resolution is generally unsatisfactory. Even at fine resolutions, the capability of *k - pdfilon* and algebraic stress models may be suspect on the basis of the 1D results of Martin (1985). As the purpose of the eddy-viscosity term is to model the introduction of momentum into the wind-mixed layer, we can substitute a model for predicting the wind-mixed

layer depth and a model for the distribution of momentum over the depth. The wind-mixed layer is the mixed layer that includes the free surface, with depth ( $h$ ) of the wind-mixed layer computed in a discrete form as:

$$h_{i,j} = \sum_{m=k_a(i,j,k_\eta)}^{k_b(i,j,k_\eta)} \Delta Z_{i,j,m} \quad (4.35)$$

where  $k_a$  and  $k_b$  are the lower and upper grid cell indices of the discrete wind-mixed layer in the water column ( $i, j$ ) that has free surface grid cell  $k_\eta$ . To first order, we can approximate the introduction of wind momentum as a uniform distribution over the mixed layer (Imberger and Patterson, 1990):

$$\left. \frac{dU}{dt} \right|_{i,j,k} = \frac{u_*^2|_{i,j,k}}{h|_{i,j}}; \eta - h < \sum_{m=1}^k \Delta z_m < \eta \quad (4.36)$$

where  $\eta$  is the free surface height in water column ( $i, j$ ). Equation 4.36 is applied separately in the  $x$  and  $y$  directions to provide a direct increase in the velocity field in the wind-mixed layer before solution of the Navier-Stokes equations.

## Surface Thermodynamics and mass fluxes

### 5.1 Introduction

The surface exchanges include heating due to short wave radiation penetration into the lake and the fluxes at the surface due to evaporation, sensible heat (i.e. convection of heat from the water surface to the atmosphere) and long wave radiation.

Short wave radiation (280nm to 2800nm) is usually measured directly. Long wave radiation (greater than 2800nm) emitted from clouds and atmospheric water vapour can be measured directly or calculated from cloud cover, air temperature and humidity. The reflection coefficient, or albedo, of short wave radiation varies from lake to lake and depends on the angle of the sun, the lake colour and the surface wave state.

### 5.2 Surface energy fluxes

**5.2.1 Solar (shortwave) radiation flux** Shortwave radiation can be divided into four components. ELCOM 2.2 assumes the following percentages for each component

- Photosynthetically Active Radiation (PAR) 45%
- Near Infrared (NIR) 41%
- Ultra Violet A (UVA) 3.5%
- Ultra Violet B (UVB) 0.5%

The distance the radiation penetrates into the water column is dependent on the extinction coefficient for each band-width. ELOCM allows users to set the extinction coefficient for each band in the run\_elcom.dat file but has the following default values

- Photosynthetically Active Radiation (PAR)  $0.25m^{-1}$
- Near Infrared (NIR)  $1m^{-1}$
- Ultra Violet A (UVA)  $1m^{-1}$
- Ultra Violet B (UVB)  $2.5m^{-1}$

If water quality is being simulated via CAEDYM then the PAR extinction coefficient is calculated by CAEDYM.

The depth of penetration of short wave radiation depends on the net short wave radiation that penetrates the water surface and the extinction coefficient. The equations given in TVA (eq 2.48 and 2.37) and Jacquet (eq A5.2) for the net solar radiation penetrating the water can be written as:

$$Q_{sw} = Q_{sw(total)}(1 - r_a^{(sw)}) \quad (5.1)$$

where  $Q_{sw(total)}$  is the short wave radiation that reaches the surface of the water on  $Q_{sw}$  is the net short wave radiation penetrating the water surface, and  $r_a^{(sw)}$  is the shortwave albedo of the water surface given by:

$$r_a^{(sw)} = \begin{cases} \bar{R}_a^{(sw)} + a_{(sw)} \sin\left(\frac{2\pi d}{D} - \frac{\pi}{2}\right) : SthHemisphere \\ \bar{R}_a^{(sw)} : Equator \\ \bar{R}_a^{(sw)} + a_{(sw)} \sin\left(\frac{2\pi d}{D} + \frac{\pi}{2}\right) : NthHemisphere \end{cases} \quad (5.2)$$

and  $\bar{R}_a^{(sw)} = 0.08$ ,  $a_{(sw)} = 0.02$ ,  $D <$  the standard number of days in a year ( $= 365$ ) and  $d$  is the day number in the year.

Short-wave radiation in each band penetrates according to the Beer-Lambert law, such that

$$Q(z) = Q_{sw} e^{-\eta_a z} \quad (5.3)$$

where  $x$  is the depth below the water surface and  $\eta_a$  is the attenuation coefficient for each band.

Thus, the shortwave energy per unit area entering layer  $k$  through its upper face is

$$\Delta Q_k = Q_k - Q_{k-1} \quad (5.4)$$

or

$$\Delta Q_k = Q_k (1 - e^{\eta_a \Delta Z_k}) \quad (5.5)$$

For heating purposes, it is assumed that all of the  $\Delta Q$ 's are converted to heat.

If there is excess short wave energy at the bottom of a column of water ELCOM reflect a portion of the energy back into the domain (currently 90% in Version 2.2). This energy is allowed to propagate back up through the water column according to the Beer-Lambert law.

### 5.3 Long wave energy flux

Longwave radiation is calculated by one of three methods, depending on the input data. Three input measures are allowed: incident long wave radiation, net long wave radiation, and cloud cover.

**5.3.1 Incident long wave radiation:** Using incident long wave radiation requires accounting for albedo and long wave radiation emitted from the water surface. The long wave radiation penetrating the water surface is then

$$Q_{lw} = (1 - r_a^{(lw)}) Q_{lw(incident)} \quad (5.6)$$

where  $r_a^{(lw)}$  is the albedo for long wave radiation, which is taken as a constant  $= 0.03$  (Henderson-Sellers, 1986).

Long wave radiation emitted from the water surface is given by (Tennessee Valley Authority (1972), eqn 3.5)

$$Q_{lw(emitted)} = .pdfilon_w \sigma T_w^4 \quad (5.7)$$

where  $.pdfilon_w$  is the emissivity of the water surface ( $=0.96$ ),  $\sigma$  is the Stefan-Boltzmann constant ( $\sigma = 5.6697 \times 10^{-8} \text{ W m}^{-2} \text{ K}^{-4}$ ), and  $T_w$  is the absolute temperature of the water surface (i.e. the temperature of the surface layer).

The nett longwave radiation energy density deposited into the surface layer for the period  $\Delta t$  is therefore

$$Q_{lw} = (1 - r_a^{(lw)})Q_{lw(incident)} - .pdfilon_w \sigma T_w^4 \quad (5.8)$$

**5.3.2 Nett long wave radiation:** Using net long wave radiation requires accounting for albedo at the water surface. The long wave radiation energy density deposited into the surface layer for the period  $\Delta t$  is therefore

$$Q_{lw} = (1 - r_a^{(lw)})Q_{lw(nett)} \quad (5.9)$$

**5.3.3 Cloud cover:** Long wave radiation can also be estimated from atmospheric conditions, using cloud cover fraction ( $0 \leq C \leq 1$ ). The nett long wave radiation energy density incident on the water surface can be estimated as

$$Q_{lw(rad)} = (1 - r_a^{(lw)})Q_{lw(air)} \quad (5.10)$$

where (Tennessee Valley Authority (1972), eqn 3.14, Fischer et al. (1979) eqn 6.21);/P;

$$Q_{lw(air)} = (1 + 0.17C^2).pdfilon_a(T_a)\sigma T_a^4 \quad (5.11)$$

the subscript  $a$  referring to properties of the air. Swinbank (1963) showed that

$$.pdfilon_a(T_a) = C.pdfilon T_a^2 \quad (5.12)$$

where  $C.pdfilon = 9.37 \times 10^{-6} \text{ K}^{-2}$ . As previously, the long wave emitted is

$$Q_{lw(emitted)} = .pdfilon_w \sigma T_w^4 \quad (5.13)$$

The nett long wave radiation is therefore

$$Q_{lw} = (1 - r_a^{(lw)})(1 + 0.17C^2).pdfilon_a(T_a)\sigma T_a^4 - .pdfilon_w \sigma T_w^4 \quad (5.14)$$

## 5.4 Sensible heat flux

The sensible heat loss from the surface of the lake for the period  $\Delta t$  may be written as (Fischer et al. (1979) eqn 6.19)

$$Q_{sh} = C_S \rho_a C_P U_a (T_a - T_s) \Delta t \quad (5.15)$$

where  $C_S$  is the sensible heat transfer coefficient for wind speed at 10 m reference height above the water surface ( $= 1.3 \times 10^{-3}$ ),  $\rho_a$  the density of air in  $kgm^{-3}$ ,  $C_P$  the specific heat of air at constant pressure ( $= 1003 Jkg^{-1}K^{-1}$ ),  $U_a$  is the wind speed at the 'standard' reference height of 10m in  $ms^{-1}$ , with temperatures either **both** in Celsius or **both** in Kelvin.

## 5.5 Latent heat flux

The evaporative heat flux is given by (Fischer et al. (1979) eqn 6.20)

$$Q_{lh} = \min \left( 0, \frac{0.622}{P} C_L \rho_a L_E U_a (e_a - e_s(T_s)) \Delta t \right) \quad (5.16)$$

where  $P$  is the atmospheric pressure in pascals,  $C_L$  is the latent heat transfer coefficient ( $= 1.3 \times 10^{-3}$ ) for wind speed at the reference height of 10 m,  $\rho_a$  the density of air in  $kgm^{-3}$ ,  $L_E$  the latent heat of evaporation of water ( $= 2.453 \times 10^6 Jkg^{-1}$ ),  $U_a$  is the wind speed in  $ms^{-1}$  at the reference height of 10m,  $e_a$  the vapour pressure of the air, and  $e_s$  the saturation vapour pressure at the water surface temperature  $T_S$ ; both vapour pressures are measured in pascals. The condition that  $Q_{lh} \leq 0$ , is so that no condensation effects are considered.

The saturated vapour pressure  $e_s$  is calculated via the *Magnus – Tetens* formula (Tennessee Valley Authority (1972), eqn 4.1):

$$e_s(T_s) = 100 \exp \left[ 2.3026 \left( \frac{7.5 T_s}{T_s + 237.3} + 0.758 \right) \right] \quad (5.17)$$

where  $T_s$  is in degrees Celsius and  $e_s$  is in pascals.

Thus, the total non-penetrative energy density deposited in the surface layer during the period  $\Delta t$  is given by

$$Q_{non-pen} = Q_{lw} + Q_{xh} + Q_{lh} \quad (5.18)$$

## 5.6 Surface mass fluxes

**5.6.1 Latent heat mass flux density** The change in mass in the surface layer cells (layer number  $N$ ) due to latent heat flux is calculated as

$$\Delta M_N^{lh} = \frac{-Q_{lh} d_x d_y}{L_V} \quad (5.19)$$

where  $d_X$  and  $d_Y$  are the grid size of the surface layer cell and  $L_V$  is the latent heat of vaporisation for water.

**5.6.2 Rainfall** It is assumed that the temperature of the rain is the same as that of the surface cell. The salinity and water quality are set to zero. The change in surface layer mass is

$$\Delta M_N^{rain} = \rho_{rain} d_X d_Y r \Delta t \quad (5.20)$$

where  $r$  is the rainfall in  $m s^{-1}$

## 5.7 Atmospheric stability and surface exchange

One factor known to cause variability in the heat and momentum transfer described above is air column stability and water roughness (Imberger and Patterson, 1990). This has the effect of altering the exchange coefficients  $C_S$ ,  $C_L$  and  $C_D$ .

If the meteorological sensors are located within the internal boundary layer over the surface of the lake, and data is collected at sub-daily intervals, it is appropriate to consider the effect of air column stability on surface exchange. ELCOM uses the iterative procedure of Hicks (1975) to compute these values, as described in Imberger and Patterson (1990) (p329). The user is referred to these references for more information.



## Mixing Model

### 6.1 Introduction

ELCOM models the vertical Reynolds stress terms (and thus the turbulent fluxes) in momentum and transport equations with a 3D mixed-layer approach derived from the mixing energy budgets developed for 1D lake modeling (Imberger and Patterson (1981) , Spigel et al. (1986) , Imberger and Patterson (1990)). Whereas 1D mixed-layer models are typically Lagrangian, regriding the vertical domain to match the number of mixed regions in the water column, the present 3D method uses an Eulerian fixed-grid framework as Lagrangian 3D methods typically obtain highly skewed grid cells when horizontal gradients in mixing occur. The present model applies a separate 1D mixed-layer model to each water column to provide vertical turbulent transport, whereas 3D transport of TKE is used to provide the dynamic effect of 3D motions on the TKE available for vertical mixing.

### 6.2 Energy terms in the mixed layer model

To understand the present mixed-layer approach, it is useful to qualitatively define some of the energy fluxes. First, we can characterize four energy terms:

1. The TKE available for mixing,  $TKE_A$
2. The TKE required for mixing,  $E_{req}$
3. The TKE dissipated,  $E_{dissipation}$  and
4. The residual mixing energy,  $E_M$  .

Of these, only the last, which is effectively the sum of the others at the end of the mixing algorithm, is considered a transported variable. Second, it is useful to characterize two types of mixing events in a stratified fluid:

1. convective mixing of unstable density gradients that decreases the potential energy of the fluid and releases TKE
2. mixing of stable density gradients that dissipates TKE and increases potential energy.

The former is one of the TKE sources for mixing ( $TKE_A$ ), whereas the latter is exactly the local energy required to mix ( $E_{req}$ ). These two density gradient terms are computed from the vertical buoyancy scale, with the magnitude of a negative value providing the convective contribution to  $TKE_A$  and a positive value providing  $E_{req}$ . The distinction between the positive and negative forms of the buoyancy scale is critical to the model, as an unstable density gradient will always create  $TKE_A$  , whereas a stable gradient ( $E_{req} > 0$  ) will consume  $TKE_A$  only when  $TKE_A < E_{req}$  . Finally, we need a definition for a 'mixed layer'; this is taken to be a set of vertically contiguous grid cells that share the same density, scalar concentrations, and grid-scale velocity. According to this

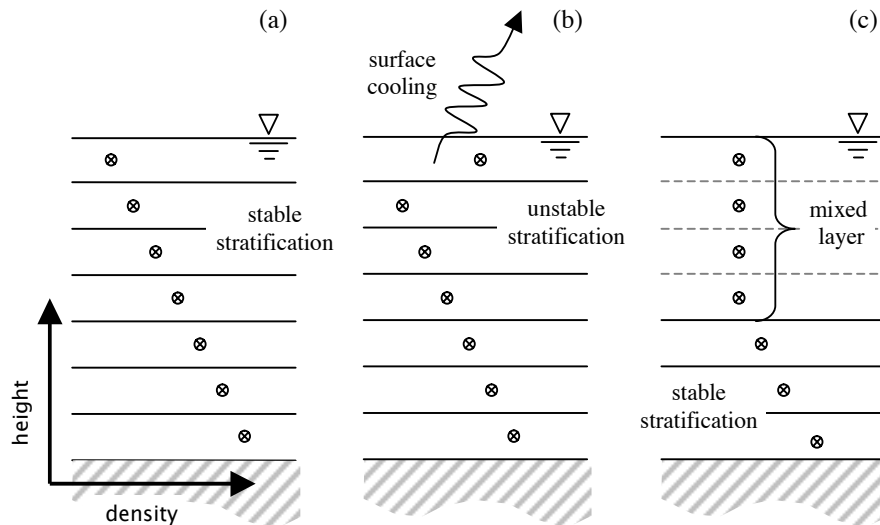


Figure 6.1 Development of a mixed layer due to surface cooling and unstable stratification. (a) Stable stratification at start of time step; (b) surface cooling creates unstable density profile; (c) unstable grid cells have been mixed.

definition, the discrete version of a linear stratification with seven grid cells shown in Figure. 6.1a is a system with seven mixed layers, whereas the system in Figure. 6.1c has the same number of vertical grid cells but only four mixed layers. Note that in this mixed-layer model, the layers do not have a dynamical existence outside the mixing algorithm and do not carry forward from time step to time step. That is, when the mixing routine is called, the layers are computed from the present density structure and mixing energy without explicit reference to any prior layer structure.

The present approach is considerably simpler than many 1D models (e.g., Spigel et al. (1986)) in that differential equations coupling layer thickness, entrainment rates, and heat transfer through the surface are not used. The fundamental presumption of our modeling approach is that the vertical grid resolution for practical 3D lake models is too coarse to adequately compute the solution of differential equations for mixed-layer evolution or heat transfer with gradient boundary conditions. Indeed, the need to model with coarse vertical grid resolution was the impetus for abandoning the vertical eddy-diffusion differential equations generally used for mixing. The surface thermodynamics in ELCOM enter the system as discrete changes to the temperature structure in the upper grid cells rather than as boundary conditions on transport or mixing equations. At the beginning of a time step, nonpenetrative heat flux (e.g., long-wave radiation, convective heat transfer) is added to the uppermost grid cell while solar radiation is added to the water column using exponential decay over depth. The heat transfer changes the density stratification, either providing  $TKE_A$  (unstable density gradients produced by net cooling) or increasing  $E_{req}$  (stable stratification produced by net warming). Once the new density field is calculated, the mixing process is modeled on a layer-by-layer basis through each  $(i, j)$  water column by comparing the available mixing energy ( $TKE_A$ ) from convective

overtuns, shear production, wind stirring, and TKE storage ( $E_M$ ) to the potential energy increase ( $E_{req}$ ) required to mix a grid cell up into the mixed layer above itself. This mixing process is explained in the following section.

### 6.3 A Mixing timestep

A mixing model timestep for each column of water can be broken down in to the following s.pdf

1. Calculate wind energy input,  $E_{wind}$
2. If the TBBL boundary condition is being used calculate bottom energy input,  $E_{drag}$
3. For each column cycle from surface cell to bottom cell
4. Calculate generation of TKE by shear,  $E_{shear}$
5. Calculate energy required for mixing,  $E_{req}$
6. Calculate total energy available if two cells were totally mixed,  $TKE_{mixed}$
7. Calculate time estimate for total mixing  $T_{TKE}$
8. If unstable calculate time estimate based on convective overturn  $T_{conv}$
9. Calculate mixing fraction  $\eta_f$
10. If there is enough energy then mix cells
11. End of cycle from surface cell to bottom cell
12. Dissipate excess mixing energy

1. Wind Energy:

Wind generation of TKE is parameterised as

$$E_{wind} = \frac{1}{2} C_n^3 dt u_*^3 \quad (6.1)$$

Where  $u_*$  is the wind shear velocity given by

$$u_* = \sqrt{\frac{C_D^{wind} \rho_{air}}{\rho_0} U_{wind}} \quad (6.2)$$

and the mixing coefficient  $C_n$  is set to 1.33. The wind energy for each column is added to the available TKE of the surface cell.

$$TKE_{surf} = TKE_{surf} + E_{wind} \quad (6.3)$$

## 2. Bottom Energy:

If the `DEFAULT_BC` is set to `TBBL` then TKE is also generated due to drag on the bottom. This energy is parameterised as

$$E_{drag} = C_b(|u_{bot}| + |v_{bot}|)^3 dt \quad (6.4)$$

the mixing coefficient  $C_b$  is set to 2.2. The bottom energy for each column is added to the available TKE of the bottom cell.

$$TKE_{bot} = TKE_{bot} + E_{drag} \quad (6.5)$$

## 3. Begin Cycle from surface to bottom:

Once the external energy sources have been added to the surface and bottom cells the main mixing routine is called. This routine loops from the surface cell to the bottom cell and generates the mixing layers for the column.

The loop first sets the surface cell ( $k_{surf}$ ) to a mixed layer and attempts to mix the cell  $k_{surf} - 1$  into this mixed layer. If there is enough energy to mix the cells and  $\Delta t$  is large enough for the cell to be fully mixed ( $\eta_f = 1$ ) then the cells are mixed  $k_{surf} - 1$  is added to the mixed layer and then we attempt to mix  $k_{surf} - 2$  with the mixed layer. If there is not enough energy for mixing to occur or  $\eta_f < 1$  then the mixed layer is closed, ( $k_{surf} - 1$ ) is set to a mixed layer and energy budgets are computed for  $k_{surf} - 2$ . If there is enough energy for mixing to occur but the mixing fraction is  $< 1$  then partial mixing occurs.

## 4. Shear Energy:

Shear generation of TKE is parameterised as

$$E_{shear} = \frac{1}{2} C_s S^2 dz_l \quad (6.6)$$

the mixing coefficient  $C_s$  is set to 0.15 and  $S$  is the shear defined as

$$S^2 = (U_{ml} - U_l)^2 + (V_{ml} - V_l)^2 \quad (6.7)$$

subscripts  $ml$  refer to values in the mixed layer and subscripts  $l$  refer to the cell directly below the mixed layer *ie.* the cell that we are checking to see if it will become part of the mixed layer. Shear energy is stored in the cell that is being mixed into the mixed layer.

## 5. Potential Energy:

The energy required to mix the current cell into the mixed layer is given by

$$E_{req} = -g' dz_l dz_{ml} \quad (6.8)$$

where the reduced gravity term is given by

$$g' = \frac{1}{2} g (\rho_{ml} - \rho_l) \frac{(dz_{ml} dz_l)}{\rho_{ml} (dz_{ml} + dz_l) \rho_l} \quad (6.9)$$

$dz_{ml}$  is the mixed layer depth given by the sum of all the  $dz$  of cells in the mixed layer.

## 6. Total Available TKE Energy:

To determine a timescale for the mixing we first determine the total amount of energy if the cell of interest is completely mixed into the mixing layer. If the density profile is unstable then energy generated from convective overturns is added. The total  $TKE$  is then

$$TKE_{mixed} = \begin{cases} TKE_{ml} + TKE_l + E_{shear} & \text{if } E_{req} \geq 0 \\ TKE_{ml} + TKE_l + E_{shear} - C_C E_{req} & \text{if } E_{req} < 0 \end{cases} \quad (6.10)$$

the mixing coefficient  $C_c$  is set to 0.2. The  $TKE$  of the mixed layer ( $TKE_{ml}$ ) and the cell ( $TKE_l$ ) include energy from wind stirring and bottom drag as detailed above.

## 7. Timescale for mixing due to turbulence

To try and limit the time step dependence on mixing we introduce a timescale for the mixing to occur. If this timescale is larger than the timestep used then partial mixing occurs. The time scale due to turbulent mixing is given by

$$T_{turb} = C_{TT} dz_l \sqrt{\frac{C_s dz_{ml} + dz_l}{2TKE_{mixed}}} \quad (6.11)$$

the coefficient  $C_{TT}$  is set to 50.0.

## 8. Timescale for mixing due to convective overturn

If the density profile is unstable then we introduce a timescale for overturning.

$$T_{conv} = C_{TC} dz_l \sqrt{\frac{dz_l}{g'}} \quad (6.12)$$

If the time scale for overturning is shorter than the timescale for mixing due to turbulence then we use this timescale to calculate our mixing fraction.

## 9. Calculate mixing fraction.

The mixing fraction is simply the timestep  $\Delta t$  divided by the shorter of the two timescales. The mixing fraction is limited to 1.0.

$$\eta_f = \min\left(\frac{\Delta t}{\min(T_{TKE}, T_{conv})}, 1.0\right) \quad (6.13)$$

## 10. Energy Budget.

Before any mixing takes place the mixing routine checks to see if there is sufficient  $TKE$  available to overcome the potential energy. If  $TKE_{mixed} \geq \eta_f E_{req}$  the mixing takes place using the calculated mixing fraction. If  $TKE_{mixed} < E_{req}$  no mixing occurs, the available  $TKE$  is dissipated completely and the mixed layer is closed. For complete mixing any excess  $TKE$  (ie.  $TKE_{mixed} - E_{req}$ ) is stored in the mixed layer and is included in the energy budget for the next layer. For partial mixing excess  $TKE$  is stored proportionally by volume in the mixed layer and the cell being mixed.

## 11. Mixing of cell into mixed layer.

The mixing of cells depend on whether the cells are fully or partially mixed. If  $\eta_f = 1$  all scalar and velocity values within the mixed layer are equal. Scalar concentrations are mixed by volume such that

$$C'_{ml} = \frac{C_{ml}dz_{ml} + C_l dz_l}{dz_{ml} + dz_l} \quad (6.14)$$

Where the  $C_{ml}$  is the scalar concentration of the mixed layer and  $C_l$  is the scalar concentration of the cell being mixed. The  $'$  indicates the value after mixing.

Velocities are mixed by mass such

$$U'_{ml} = \frac{\rho_{ml}U_{ml}dz_{ml} + \rho_l U_l dz_l}{\rho_{ml}dz_{ml} + \rho_l dz_l} \quad (6.15)$$

.

For partial mixing only the cell being mixed and the cell at the bottom of the mixed layer are modified.

$$C_k = \begin{cases} C_{ml} & k = k_l + 2 : k_{ml-top} \\ (1 - \eta_f)C_{ml} + \eta_f \frac{C_{ml}dz_k + C_l dz_l}{dz_k + dz_l} & k = k_l + 1 \\ (1 - \eta_f)C_l + \eta_f \frac{C_{ml}dz_{k+1} + C_l dz_l}{dz_{k+1} + dz_l} & k = k_l \end{cases} \quad (6.16)$$

where  $C_k$  is the concentration of layer  $k$  in the column,  $k_l$  refers to the layer of the cell being mixed and  $k_{ml-top}$  is the layer of the top of the mixed layer. An analogous expression to 6.15 is used for partial mixing of velocity.

12. End of cycle from surface cell to bottom cell:

Once the bottom cell is reached the cycle is concluded.

13. Dissipation of energy: After the mixing of cells has concluded excess energy is dissipated according to

$$TKE = TKE - \frac{1}{2}C_{.pdfilon}\Delta t \left( \frac{TKE}{dz} \right)^{\frac{3}{2}} \quad (6.17)$$

.

where the dissipation coefficient  $C_{.pdfilon}$  is set to 1.15. Any  $TKE$  left after dissipation is then transported by the scalar transport routine before becoming available for mixing in the following timestep.



## Numerical Diffusion Filter

This chapter describes a technique for maintaining vertical density stratification over seasonal timescales. The technique involves estimating the numerical diffusion of mass occurring in each time-step and applying a compensating correction to the density field. Since advection does not change background potential energy,  $E_b$  (Winters et al., 1995) it follows that  $E_b$  during advection must be entirely due to numerical diffusion (in the absence of inflows/ outflows). As ELCOM employs an operator splitting solution of the scalar transport equation,  $E_b$  can be calculated before and after advection to quantify numerical diffusion of mass. This method has two shortcomings. 1) The measure is global, thus it does not provide a spatial distribution of diffusion. 2) The current implementation does not allow inflows/ outflows that affect  $E_b$ . The first drawback is inherent in the methodology and can only be addressed in an approximate manner, while the second drawback could be exactly removed by quantifying the buoyancy flux of inflows/outflows. In this paper we concentrate on the first problem by developing a method to approximately redistribute  $E_b$  for domains with no inflows/outflows. The problems associated with inflows/outflows remain a subject for further research. The contribution of this paper is a methodology for using  $E_b$  to reconstruct a density field that minimizes numerical diffusion. Mathematically, we desire a correction technique that satisfies:

$$\frac{\{E_b^+\} - E_b^-}{E_b^-} < .pdfilon_B \quad (7.1)$$

at each time-step.  $E_b^-$  and  $E_b^+$  are the background potential energy before and after the transport calculation respectively. The curly braces above and hereinafter represent the application of a correction technique. The threshold  $.pdfilon_B$  is based on the capabilities of the method and represents the minimum expected reduction in numerical diffusion. In a numerical simulation of a lake, density stratification varies smoothly and monotonically with depth and, to first order, can be characterized as two weakly stratified regions (an epilimnion and a hypolimnion), separated by a strongly stratified metalimnion. The observed effect of numerical diffusion is thickening of the metalimnion. Thus, the cumulative effect is similar to vertical diffusion from the metalimnion. To first order, mitigating numerical diffusion is achieved through an anti-diffusion vertical mass flux, which is applied herein using a sharpening filter acting vertically on the density profile in each water column.

The sharpening filter was previously developed to enhance field instrument response (Fozdar et al., 1985). It is a three point recursive filter based on the inverse Z-transform of a linear response to a Heaviside step function, and is represented as follows:

$$\{S_k\} = \frac{1 - a'}{1 - a} (S_k - S_{k-1}) + a' \{S_{k-1}\} \quad (7.2)$$

where  $a = e^{-\frac{\Delta z}{l}}$ ,  $a' = e^{-\frac{\Delta z}{l'}}$ ,  $\Delta z$  is the vertical grid spacing,  $l$  and  $l'$  are sharpening and smoothing length

scales respectively,  $k$  is a grid cell index,  $S_k$  is a series value before application of the filter,  $\{S_k\}$  is a series value after application of the filter. To simulate the bi-directionality of diffusion in one dimension the filter is applied both upwards and downwards.

One problem with the original sharpening filter is gradient amplification at boundaries, which creates artificial minima and maxima. Where such extrema are unstable density gradients, they must be mixed in a hydrostatic model. Where such extrema are stable density gradients, they increase the TKE required for mixing. The cumulative effects are maximum and minimum values of density beyond the original values, and distortion of mixing dynamics. To correct this effect, an endpoint limiter and gradient preservation are applied after filtering. The gradient before filtering is calculated for both the top and bottom of each water column. After filtering, top and bottom gradients are restored to pre-filter values. After gradient correction any new extrema are restored to pre-filtering values. Applying this endpoint gradient preservation and extrema limiter adversely affects mass conservation and raises the minimum practical threshold,  $E_b$ . Since changes per time-step are extremely small, a simple mass correction is applied to evenly remove the change in mass incurred by the filtering. The change in mass due to filtering is divided by the number of cells containing less than average mass. That change in mass per cell is then subtracted from cells containing less than average mass. By applying mass correction before the extrema limiting, no new extrema are created, and the mass redistribution has the effect of further sharpening the overall stratification.

## Underflow Model

### 8.1 Introduction

The underflow model in ELCOM is based on the numerical approach proposed by Bradford and Katapodes (1999) with finite-volume spatial discretization, conservation equations advanced by a predictor-corrector algorithm and Roe (1981) approximate Riemann solver for fluxes through cell faces. The conservation equations of Bradford and Katapodes (1999) have been modified to use salinity and temperature instead of turbidity, and terms have been added to model 1) effects of the earth's rotation, 2) gradients in ambient fluid salinity and 3) momentum of the background circulation. The entrainment relationship has been changed from to the formulation of Dallimore et al. (2001), developed from a parameterisation of the turbulent kinetic energy equation. The general grid transformations of Bradford and Katapodes (1999) are replaced with a simple Cartesian-grid approach for compatibility with the Cartesian grid in ELCOM.

### 8.2 Governing Equations

The underflow model governing equations are the vertically-integrated equations of volume, momentum and salinity based on derivations of Ellison and Turner (1959). Assuming unity values for the shape factors while including the ambient fluid properties, the conservation equation of volume, x momentum, y momentum and salinity are respectively given by

$$\frac{d(H)}{dt} + \frac{d(UH)}{dx} + \frac{d(VH)}{dy} = E\sqrt{U^2 + V^2} \quad (8.1)$$

$$\frac{d(UH)}{dt} + \frac{d(U^2H)}{dx} + \frac{d(UVH)}{dy} = fVH - C_D U \sqrt{U^2 + V^2} - \frac{1}{2} \frac{d(g'H^2)}{dx} - g'HS_x + U_{amb}E\sqrt{U^2 + V^2} \quad (8.2)$$

$$\frac{d(VH)}{dt} + \frac{d(UVH)}{dx} + \frac{d(V^2H)}{dy} = -fUH - C_D V \sqrt{U^2 + V^2} - \frac{1}{2} \frac{d(g'H^2)}{dy} - g'HS_y + V_{amb}E\sqrt{U^2 + V^2} \quad (8.3)$$

$$\frac{d(SH)}{dt} + \frac{d(SUH)}{dx} + \frac{d(SVH)}{dy} = S_{amb}E\sqrt{U^2 + V^2} \quad (8.4)$$

where  $H$  is the height of the underflow;  $U$  and  $V$  are vertically averaged velocities in the  $x$  and  $y$  directions;  $S$  is the vertically averaged salinity;  $g'$  is the reduced gravity term  $= g(\rho - \rho_{amb})/\rho_{amb}$ ,  $f$  is the Coriolis parameter;  $C_D$  is the bottom drag coefficient;  $E$  is the entrainment coefficient and  $S_x$  and  $S_y$  are the bottom slopes in the  $x$  and  $y$  directions. The subscripts  $amb$  refer to the ambient value of the variable. Ambient values used by the underflow model are obtained from the salinity and velocity at the bottom boundary cells of the 3D model, and are used to model entrainment through the last terms in the momentum and salinity equations.

The entrainment coefficient ( $E$ ) in the governing equations is given by the entrainment law of Dallimore et al. (2001). The equation has been altered to account for the ambient flow and is given by

$$E = \frac{C_K C_D^{3/2} + C_s \left( \frac{\Delta u}{\sqrt{U^2 + V^2}} \right)^{3/2}}{Ri + 10 \left( C_K C_D^{3/2} + C_s \left( \frac{\Delta u}{\sqrt{U^2 + V^2}} \right)^{3/2} \right)} \quad (8.5)$$

where

$$\Delta u = \sqrt{(U^2 - U_{amb}^2) + (V^2 - V_{amb}^2)} \quad (8.6)$$

and  $Ri$  is the bulk Richardson number given by

$$Ri = \frac{g'H}{U^2 + V^2} \quad (8.7)$$

The parameterisation constants  $C_K$  and  $C_S$  account for the bottom production and shear production terms respectively.

### 8.3 Model Implementation

The model is implemented using a finite-volume method. The predictor-corrector scheme (explicit prediction and implicit correction) as outlined by Bradford and Katapodes (1999) is used to obtain second-order temporal accuracy. The predictor solution is obtained from the primitive form of the governing equations. Following Bradford and Katapodes (1999), the primitive forms of governing equations are used for computational efficiency and can be written as:

$$\frac{dH}{dt} + U \frac{dH}{dx} + H \frac{dU}{dx} + V \frac{dH}{dy} + H \frac{dV}{dy} = E \sqrt{U^2 + V^2} \quad (8.8)$$

$$\frac{dU}{dt} + g' \frac{dH}{dx} + U \frac{dU}{dx} + \frac{1}{2} H \frac{dg'}{dx} + V \frac{dU}{dy} = \frac{1}{H} \left( U_{amb} E \sqrt{U^2 + V^2} - C_D U \sqrt{U^2 + V^2} \right) + fVH - gS_x \quad (8.9)$$

$$\frac{dV}{dt} + g' \frac{dH}{dy} + V \frac{dV}{dy} + \frac{1}{2} H \frac{dg'}{dy} + U \frac{dV}{dx} = \frac{1}{H} \left( V_{amb} E \sqrt{U^2 + V^2} - C_D V \sqrt{U^2 + V^2} \right) - fUH - gS_y \quad (8.10)$$

$$\frac{dS}{dt} + U \frac{dS}{dx} + V \frac{dS}{dy} = \frac{1}{H} (S - S_{amb}) E \sqrt{U^2 + V^2} \quad (8.11)$$

An approximate (predictor) solution for the conservation of volume at time  $t + \Delta t/2$  in cell  $i$ , equation is given by

$$H_{i,j}^{n+1/2} = H_{i,j}^n - \frac{\Delta t}{2} \left[ U \frac{\overline{\Delta H}_x}{\Delta x} + V \frac{\overline{\Delta H}_y}{\Delta y} + H \frac{\overline{\Delta U}_x + \overline{\Delta U}_y}{\Delta x} - E \sqrt{U^2 + V^2} \right]_{i,j}^n \quad (8.12)$$

where superscripts represent the time step and subscripts represent the center of a grid cell in the horizontal underflow model grid. Note that  $n+1/2$  represents the computational time of the predictor step. Similar expressions (not shown for brevity) can be written for predictor conservation equations of salinity and momentum. Overbars in 8.12 denote average gradients at the cell center computed from gradients across the cell faces in the  $x$  and  $y$  directions. For example

$$\overline{\Delta H_x} = \text{avg}(H_{i,j} - H_{i-1,j}, H_{i+1,j} - H_{i,j}) = \text{avg}(a, b) \quad (8.13)$$

where the averaging function used in the underflow model is the  $\beta$  family of averages given by

$$\overline{\Delta H_x} = \begin{cases} \text{sign}(a) \min(\max(|a|, |b|), \beta \min(|a|, |b|)) & ab > 0 \\ 0 & ab \leq 0 \end{cases} \quad (8.14)$$

For all simulations,  $\beta$  is equal to two, which corresponds to a Superbee averaging function.

The corrector solution is a coupled, implicit solution of a discrete form of the conservative governing equations using the predictor-step fluxes. For example, the conservation of volume equation can be written as

$$\Delta x \Delta y \frac{H^{n+1} - H^n}{dt} = F_F^{n+1/2} \Delta y + F_B^{n+1/2} \Delta y + F_R^{n+1/2} \Delta x + F_L^{n+1/2} \Delta x + E \sqrt{U^{(n+1/2)^2} + V^{(n+1/2)^2}} \quad (8.15)$$

where  $F_F$ ,  $F_R$ ,  $F_B$  and  $F_L$  are the volume fluxes through the front, right, back and left cell faces respectively. Here the nomenclature is consistent with the ELCOM code, where the front is the cell face in the positive  $x$  direction, back is in negative  $x$ , right is positive  $y$ , and left is negative  $y$ . The fluxes are defined as positive in the direction of increasing computational coordinates.

The fluxes at each cell face are calculated using the approximate Riemann solver developed by Roe (1981). These fluxes are given by

$$F_{F(i,j)} = F_{B(i+1,j)} = \frac{1}{2} \left( f_{F(i,j)}^{n+1/2} + f_{B(i+1,j)}^{n+1/2} - \hat{R} |\hat{\Lambda}| |\Delta \hat{V}| \right) \quad (8.16)$$

where the  $f_{F(i,j)}$  and  $f_{B(i+1,j)}$  refer to the estimated fluxes at the front face of cell  $(i, j)$  and the back face of  $(i+1, j)$  respectively. The third term on the right hand side is the Riemann flux term. The estimated fluxes at the front of cell  $(i, j)$  are determined from the extrapolation of the primitive variables at the centre of the cell to the front face of the cell. For example the height at the front face of cell  $(i, j)$  is given by

$$H_{F(i,j)}^{n+1/2} = H_{(i,j)}^{n+1/2} + \frac{1}{2} \overline{\Delta H_x}_{i,j}^n \quad (8.17)$$

and the estimated volume flux at the front face of cell  $(i,j)$  is given by

$$f_{F(i,j)}^{n+1/2} = H_{F(i,j)}^{n+1/2} U_{F(i,j)}^{n+1/2} \quad (8.18)$$

Similar expressions can be written for the other faces and fluxes.

In matrix form the Riemann flux terms. See Dallimore et al. (2001) and Bradford and Katapodes (1999) for more information on these terms.

Two boundary conditions are used in the underflow model, solid wall and inflow. Inflows are implemented using ghost cells located outside the computational domain. The specified flow rate, salinity and underflow height are placed within the ghost cell for each timestep. Within the ghost cell all gradient terms are set to 0. The fluxes through the interface between the ghost cell and the interior cell are calculated using the Riemann solver as described above. Solid wall boundaries are cell faces where the fluxes are set to zero.

#### 8.4 Front tracking

Following Bradford and Katapodes (1999) a front-tracking scheme is used to eliminate artificial propagation of the density front resulting from discretization. Cells in the underflow model are defined as being 'underflow', 'ambient' or 'frontal'. 'Underflow' cells are cells that are filled by the underflow; 'ambient' cells contain ambient water without underflow water, while 'frontal' cells are the boundary cells between the underflow and the ambient fluid that contain both types of water. In a frontal cell, fluxes are only calculated for faces that are bounded by an underflow cell. The front propagation distance in the  $x$  direction,  $X_f$ , from time  $n$  to  $n + 1$  within a frontal cell is given by

$$X_f^{n+1} = X_f^n + U_f^{n+1} \Delta t \quad (8.19)$$

where  $U_f$  is the front velocity. An analogous formula is used for the frontal distance in the  $y$  direction. If  $X_f^{n+1}$  is greater than the grid dimension ( $\Delta x$ ) then the cell is changed to an underflow cell and any adjacent ambient cell becomes new frontal cell. While the concept is straightforward in one dimension, in 2D a cell may be frontal cell with respect to both the  $x$  and  $y$  coordinate directions. This is simply a bookkeeping problem for the model, that is handled by designating any cell with both ambient and underflow water as a 'frontal' cell then checking whether one or two faces are involved in frontal propagation. At the end of each timestep, any ambient cell that has frontal cells on both  $x$  or both  $y$  faces is also designated as an underflow cell. This simplifies the computation for two fronts that are propagating in opposite directions and meet in a single ambient grid cell.

As pointed out by Bradford and Katapodes (1999) there are a number of possibilities for the frontal velocities  $U_f$  and  $V_f$ . We follow their approach wherein the frontal velocity is based on the computed values of  $U$  and  $V$  in the frontal cells. We add the effect of the ambient flow on front propagation by computing, the frontal velocities as

$$U_f = U + U_{amb} \quad (8.20)$$

This formulation provides a simple and robust first-order approximation for calculating the frontal propagation. Due to the explicit nature of the front-tracking scheme, the front must not propagate further than one grid cell in any timestep. If this condition is violated, the underflow model timestep is automatically halved and the underflow is recomputed. This acts recursively so that the underflow solution will always be stable. Note the timestep for the ambient 3D flow solver is not affected by the change in timestep of the underflow model.

### 8.5 Coupling the model to ELCOM

This section discusses the coupling of the 2D underflow model with the 3D solver ELCOM. As an underflow travels along the bottom boundary of a water body it has two effects on the ambient water. Firstly it entrains ambient water into itself and secondly it displaces ambient fluid away from the bottom boundary. The proposed coupling scheme attempts to model these effect via the use of inflows and outflow across the bottom boundary of the 3D domain. The fundamental idea behind the scheme is to insert the net change in the underflow volume during each timestep through the bottom boundary of the 3D domain over the appropriate cells while still tracking the salinity of the underflow with the 2D model. In effect the water that is inserted into the 3D domain is designed to acts as a 'place holder' that will be replaced with the underflow water once the underflow reaches its insertion level. A schematic of the coupling procedure is shown for a homogeneous ambient water body in 8.1. The three basic s.pdf of the scheme are:

1. Removal of the entrained water from the 3D domain (8.1a)
2. Insertion of the net volume increase in each underflow cell into the corresponding ELCOM bottom boundary cell. (8.1b)
3. Insertion of salinity once the plume has reached its level of neutral buoyancy. (8.1c and d)

S.pdf one and two are implemented every timestep, step three only occurs once the underflow reaches the insertion level.

Both the entrainment and the net change in volume of an underflow cell (8.1a) are easily calculated from the underflow model. After each underflow timestep is completed the entrained volume is removed from the appropriate cell on the bottom boundary of the 3D domain. The net change in volume of the underflow cell is then inserted into the 3D domain as an inflow across the bottom boundary of the corresponding 3D column. So as not to introduce any unwanted currents in the 3D domain this inflow is given a salinity equal to the salinity at the bottom of the ELCOM column. The idea is to insert the underflow volume over the appropriate cells while having the minimal effect on the ambient motions. In practice, because the entrained and the insertion fluid both have a salinity given by the salinity at the bottom of the 3D domain, s.pdf 1 and 2 are combined to form a single inflow for each column. The volume of the inflow is given by the change in volume of the cell minus the volume entrained into the cell

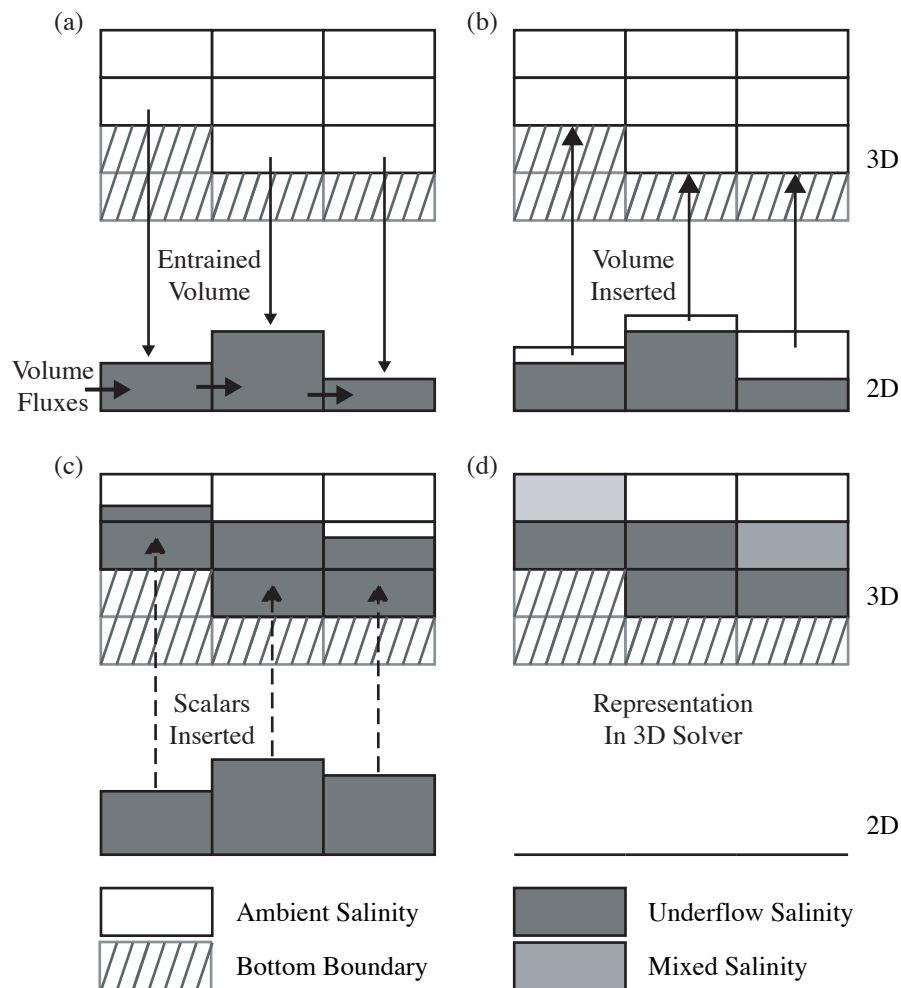


Figure 8.1 Profiles showing coupling of the 2D underflow model to the 3D solver. The net volume for each underflow cell is calculated for each timestep (a). This volume is inserted as an inflow across the bottom boundary of the 3D domain (b). Once the underflow reaches its insertion level the salinity within a volume at the bottom of each column in the 3D domain is replaced with the salinity of the underflow. (d) shows the representation of the underflow within the 3D domain after insertion.

and is equal to the net volume flux into the cell given by the modeled Riemann fluxes. If the net volume flux into the underflow cell is negative (eg: at the tail of the underflow) then the appropriate volume is removed from the ELCOM cell as an outflow.

It can easily be shown that the sum of the net volume fluxes into all underflow cells, and hence the total volume flux into ELCOM, is equal to the specified inflow flux at the side boundary. This ensures that conservation of volume is maintained in the 3D solver and that the modeled free surface height in ELCOM accurately represents the supplied inflows.

Once the underflow reaches its insertion level the salinity in the 3D domain is altered to reflect the salinity of the underflow. The criteria for insertion are defined as when any underflow body cell is less dense than the ambient ELCOM cell 'above it' or when the height of the underflow is greater than 5 times ELCOMs vertical grid size.

The idea behind the salinity insertion subroutine is to replace the salinity within a certain volume at the bottom of each column  $(i, j)$  in the 3D domain such that after the insertion the salinity in the 3D domain represents the height and salinity predicted by the underflow model at each cell  $(i, j)$ . If the 3D domain has a uniform salinity before the underflow event occurs then the insertion is trivial. For this case both the volume input at the bottom boundary of the ELCOM domain and the entrained water into the underflow have a salinity equal to the uniform ambient salinity. It can be shown that for this scenario conservation of salinity is achieved by replacing the ambient salinity at the bottom of each column  $(i, j)$  up to a height equal to the underflow height at cell  $(i, j)$  with the underflow salinity  $(S_{i,j})$ . The replacement of salinity is achieved using the following formulae:

$$S^{ELCOM} = \begin{cases} S & z_{top} < H \\ \frac{S(H-z_{bot})}{dz} + \frac{S^{ELCOM}(z_{top}-H)}{dz} & z_{top} < H \\ S^{ELCOM} & z_{bot} > H \end{cases} \quad (8.21)$$

Where  $S^{ELCOM}$  is the salinity in the ELCOM cell,  $dz$  is the vertical grid size and  $z_{top}$  and  $z_{bot}$  are the height above the bottom of the top and bottom faces of the ELCOM cell. The representation of the underflow salinity in the 3D solver after insertion is shown in 8.1d.

When the ambient salinity is not uniform the above scheme is not conservative for salinity. The problem is the total amount of salinity being replaced is not necessarily equal to the salinity that was input into the 3D domain before the time of insertion. There are two possible solutions to this; either the volume of water being replaced of the underflow salinity can be altered to arbitrarily balance salinity. In ELCOM the former was chosen for two reasons. Firstly, if the underflow salinity is changed there is the possibility that the new salinity will be unrealistically high. Secondly, because the height of the underflow in ELCOM must be an integer number of cells high a small change in the volume of water replaced in the ELCOM domain will have a small effect on the representation of the underflow within ELCOM. The height over which salinity is replaced in column is given by

$$H_{insert} = H + \frac{S_{removed} - S_{added}}{S\Delta x\Delta y} \quad (8.22)$$

Where  $S_{removed}$  is the total salinity replaced in the ELCOM column,  $S_{added}$  is the salinity that has been added through the bottom of the ELCOM column and  $H$  and  $S$  are the predicted height and salinity of the underflow. Once  $H_{insert}$  has been calculated the salinity within the 3D domain can be modified according to 8.21 above with  $H$  replaced by  $H_{insert}$ . Note that if  $S_{removed}$ , as in the ambient uniform case, 8.22 predicts an insertion height equal to the height of the underflow.

The two major parts of the insertion routine can be summarised as:

1. At each time step a volume is inserted through the bottom boundary of each column in the 3D domain. This volume is equal to the net volume flux into the corresponding underflow cell. The salinity of the inserted water is given by the salinity in the bottom cell of the ELCOM column.
2. Once the underflow has reached its level of insertion then the salinity in a certain volume at the base of every column in the 3D domain is replaced by the salinity of the corresponding underflow cell. The volume of water replaced is chosen to ensure conservation of salinity.

It should be noted that once the insertion of salinity has taken place and the tracking of the underflow has essentially been handed over to ELCOM that numerical convective entrainment will still occur. Two scenarios lead to the insertion of salinity. The first is when the height of the underflow is large compared to the vertical grid size in which case the effect of numerical mixing is small compared to the volume of the flow. The second scenario is when the underflow reaches neutrally buoyancy. For this scenario the effect of convective entrainment is reduced because as water flows over a step in the bathymetry the water below it will have a similar salinity.

## 8.6 Plunge Point Analysis

In order to model the plunging region of an inflow event a simple first-order approximation was made to the underflow model to account for the error in the momentum equation. This modification deals with the symptoms of the momentum error rather than addressing the error directly. Once the underflow volume fluxes are calculated the underflow height for each underflow cell at timestep  $n + 1$  are first estimated by neglecting the entrainment into the flow such that

$$\Delta x\Delta y \frac{H^{n+1} - H^n}{dt} = F_F^{n+1/2}\Delta y + F_B^{n+1/2}\Delta y + F_R^{n+1/2}\Delta x + F_L^{n+1/2}\Delta x \quad (8.23)$$

The predicted underflow height for each cell is then compared to the corresponding depth of the reservoir in the 3D domain. If the underflow height is greater than the water depth then the volume fluxes are manipulated so that the  $H_{n+1}$  is equal to the depth of the reservoir. More specifically the volume flux through the face in the

direction of the underflow front is increased to provide the necessary change. Scalar fluxes are altered to reflect the change in volume flux. In order to ensure that no mixing takes place before the plunge point of the underflow the entrainment coefficient for these cells is set to zero. Rather than altering the momentum equation to deal with a plunging flow, the conservation of volume equation is utilised to give

$$U^{n+1} = \frac{F_F^{n+1/2} + F_B^{n+1/2}}{H^{n+1/2}} \quad (8.24)$$

$$V^{n+1} = \frac{F_R^{n+1/2} + F_L^{n+1/2}}{H^{n+1/2}} \quad (8.25)$$

A further complication can arise during the solution of the conservation equations. The predicted height at time  $t = t + \Delta t$  is given by the conservation of volume equation

$$\Delta x \Delta y \frac{H^{n+1} - H^n}{dt} = F_F^{n+1/2} \Delta y + F_B^{n+1/2} \Delta y + F_R^{n+1/2} \Delta x + F_L^{n+1/2} \Delta x + E \sqrt{U^{(n+1/2)^2} + V^{(n+1/2)^2}} \quad (8.26)$$

If the entrainment term is large it is still possible for  $H^{n+1}$  to be greater than the depth of the water column. This is easily dealt with by modifying the entrainment coefficient,  $E$ , where the underflow height is greater than the water depth to ensure  $H^{n+1}$  is equal to the depth.



## Artificial Destratification

### 9.1 Introduction

ELCOM provides algorithms for two types of destratification devices: Bubble plums and jets. Both devices act vertically on a column of water and work by calculating the entrainment of water from each cell into the jet or plume.

Water insertion and entrainment is carried out by creating a temporary column of water with  $nz + nn$  layers. The layers consist of the original  $nz$  layers each slightly smaller than its usual  $dz$  due to entrainment into the plume and 1 inserted layer for a jet or one inserted layer for each time the bubble plume detrains. The  $dz$  of the inserted layer is given by the insertion volume divided by the column area. Once the plume calculations have been carried out the standard  $z$  layer configuration is enforced onto the temporary column. This leads to some numerical diffusion (Figure 9.1).

### 9.2 Bubble Plumes

The bubble plume destratification in ELCOM is based on the routine in DYRESM. The model uses the simple buoyant plume equations, and assumes the plumes are circular and multiple plumes in any grid cell are non-interacting. Air is pumped to depth, and released into the water column via a diffuser. The bubbles rise, entraining ambient water. When the upwards buoyancy flux due to the air bubbles is equal to the downwards force (due to gravity) of the entrained ambient water, the bubble plume sheds the entrained water. This water is immediately routed to its neutrally buoyant level, without entrainment.

The bubble plume then begins to entrain ambient water again, until it reaches the surface where any entrained water is shed, and again routed to its neutrally buoyant level.

**9.2.1 Initialisation:** The bubbler is initialised by first computing the upwards buoyancy flux due to the air, as (Fischer et al. (1979), eqn 9.7)

$$B_{air} = gQ_{diff} \quad (9.1)$$

Note that the air flow rate MUST be that at the level of the diffuser, not the free-air flow rate of the compressor. The correction can be made by assuming that air is in ideal gas and is adiabatically compressed according to (Wallace and Hobbs (1977), p89)

$$Q_{diff} = Q_{air} \left( \frac{P_{air}}{P_{diff}} \right)^{0.71} \quad (9.2)$$

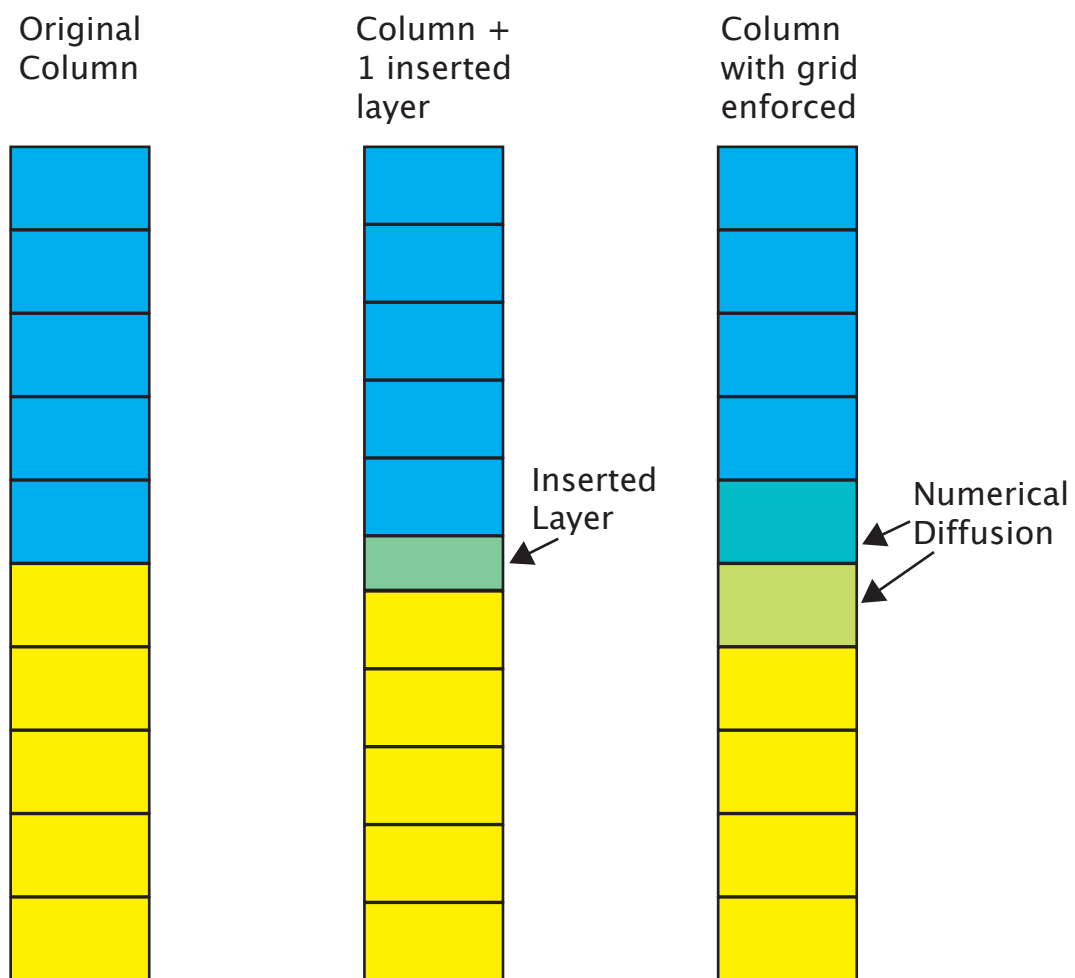


Figure 9.1 Schematic of bubble plume or jet entrainment and insertion.

where  $Q_{air}$  is the free air flow rate of the compressor,  $P_{air}$  is the air pressure (usually taken as 101.3 kPa),  $P_{diff}$  the pressure at the level of the diffuser due to both the atmosphere and the depth of water, and  $Q_{diff}$  the diffuser air flow rate.

Once the value of  $Q_{diff}$  is passed into the model, it is divided by the number of ports (or clusters) to determine the flow rate per port. All subsequent calculations are done on a per port basis, then multiplied by the total number of ports to get the total effect of the destratification system.

The flow rate of entrained water is computed as (Fischer et al. (1979), eqns 9.28, 9.30, 9.107)

$$Q_P = \alpha \frac{6\pi}{5} b_1 L_R B^{1/3} z^{5/3} \quad (9.3)$$

where  $B$  is the buoyancy flux [ $m^4/s^3$ ],  $z$  is the bottom layer thickness [ $m$ ],  $b_1$  is a constant (= 4.7 Fischer et al. (1979), p329),  $L_R$  is the plume aspect ratio (plume radius to plume length, assumed to be a constant of 0.1), and  $\alpha$  is an entrainment coefficient.

**9.2.2 Subsequent entrainment:** The first step is to compute the flow rate of air, which will increase due to decreasing pressure leading to adiabatic expansion of the bubbles. The new flow rate (due to adiabatic expansion) in layer  $k$  can be calculated as

$$Q_i = Q_{i-1} \left( \frac{P_{i-1}}{P_i} \right)^{0.71} \quad (9.4)$$

where layer  $(k - 1)$  refers to the layer below, and pressure  $P$  has units of Pascals.

The combined buoyancy flux of the air bubbles and entrained water is calculated as

$$B_i = gQ_i - g \left( \frac{\rho_i - \rho_P}{\rho_i} \right) Q_P \quad (9.5)$$

where  $\rho_i$  is the density of the current layer, and  $Q_p$  is the flow rate of the entrained volume. The second term is the reduction in buoyancy flux due to the entrained water the plume is dragging with it.

The flow rate of the entrained volume in layer  $i$  is calculated as

$$Q_P = \alpha \frac{6\pi}{5} b_1 L_R B^{1/3} \left( z_i^{5/3} - z_{i-1}^{5/3} \right) \quad (9.6)$$

**9.2.3 Detrainment:** When the combined buoyancy flux becomes negative, the entrained water detrains from the air plume. It is then routed to its neutrally buoyant level instantaneously.

The plume characteristics are then reset, and the air continues to rise and begins entraining water again.

Water insertion and entrainment is carried out as described above (Section 9.1).

### 9.3 Pumps/Jets

The jet model uses the simple jet equations, and assumes the plumes are circular and multiple plumes in any grid cell are non-interacting. Unlike bubble plumes pumps may act up or down the water column. As the jet moves away from the pump it entrains ambient water. When the momentum flux of the jet reaches zero the the entrained water is immediately routed to its neutrally buoyant level, without entrainment.

**9.3.1 Initialisation:** The jet is initialised by first computing the momentum flux exiting the pump. The vertical velocity at the pump is given by

$$w_0 = \frac{2J}{\pi\rho_0 R} \quad (9.7)$$

Where  $J$  is the thrust of the pump in Newtons and  $R$  is the radius of the pump. The initial radius of the jet,  $b_0$  is set to the radius of the pump. The initial volume flux is therefore

$$Q_0 = \pi b_0^2 w_0 \quad (9.8)$$

The water for this volume flux is removed from cells above the pump if the pump is pumping down and below the pump if it is pumping up. The water is removed equally from all cells a distance equal to  $R$ .

**9.3.2 Subsequent entrainment:** The entrainment into the jet is calculated by explicitly solving the conservation of volume equation

$$\frac{\partial(\pi b^2 w)}{\partial z} = 2\pi b w \quad (9.9)$$

The conservation of momentum equation is then solved to calculate the vertical velocity

$$\frac{\partial(\frac{\pi}{2} b^2 w^2)}{\partial z} = \pi b g \frac{\rho_j - \rho_{amb}}{\rho_0} \quad (9.10)$$

Where  $\rho_j$  is the density of the water in the jet and  $\rho_{amb}$  is the density of the cell.

**9.3.3 Detrainment:** When the momentum flux becomes negative, the entrained water detrains from the jet. It is then routed to its neutrally buoyant level instantaneously. Water insertion and entrainment is carried out as described above (Section 9.1).

## Bibliography

- ALDERSON, S.G. 1990. On embedding a mixed layer model into an ocean general circulation model. *Dyn. Atmos. Oceans* **15**, pp. 59–86.
- AL-KHAFAJI, A.W. & TOOLEY, J.R. 1986. *Numerical Methods in Engineering Practice* Holt, Reinhart and Winston, Inc..
- AMOROCHO, J. & DEVRIES, J.J. 1980. A new evaluation of the wind stress coefficient over water surfaces. *J. Geophys. Res.* **85**, pp. 433–442.
- ANTENUCCI, J., IMBERGER, J. & SAGGIO, A. 2000. Seasonal evolution of the basin-scale internal wave field in a large stratified lake. *Limnol. Oceanogr.* **45**, pp. 1621–1638
- ASSOULINE, S. & MAHRER, Y. 1996. Spatial and temporal variability in microclimate and evaporation over Lake Kinneret: Experimental evaluation. *Appl. Meteorol.* **35**, pp. 1076–1084.
- BELETSKY, D., O'CONNOR, W.P., SCHWAB, D.J. & DIE-TRICH, D.E 1997. Numerical simulation of internal Kelvin waves and coastal upwelling fronts. *J. Phys. Oceanogr.* **27**, pp. 1197–1215
- BENNETT, S.G. 1973. A theory of large-amplitude Kelvin waves.. *J. Phys. Oceanogr.* **3**, pp. 57–60.
- BRADFORD, S.F. & KATAPODES, N.D. 1999. Hydrodynamics of turbid underflows. I: Formulation and numerical analysis. *J. Hydraul. Eng.* **125(10)**, pp. 1006–1015.
- CASULLI, V. 1997. Numerical simulation of three-dimensional free surface flow in isopycnal co-ordinates. *J. Numer. Methods Fluids.* **25**, pp. 645–658.
- CASULLI, V. & CATTANI, F.C. 1994. Stability, accuracy and efficiency of a semi-implicit method for three-dimensional shallow water flow. *Comput. Math. Applic.* **27**, pp. 99–112.
- CASULLI, V. & CHENG, R.T. 1992. Semi-implicit finite difference methods for three-dimensional shallow water flow. *Int. J. Numer. Methods Fluids.* **15**, pp. 629–648.
- CHEN, D., ROTHSTEIN, L.M. & BUSALACCHI, A.J 1994. A hybrid vertical mixing scheme and its application to tropical ocean models. *J. Phys. Oceanogr.* **24**, pp. 2156–2179
- CSANADY, G.T. 1967. Large-scale motion in the Great Lakes. *J. Geophys. Res.* **72**, pp. 4151–4162.
- DALLIMORE, C.J., IMBERGER, J & ISHIKAWA, T. 2001. Entrainment and Turbulence in Saline Underflow in Lake Ogawara. *J. Hydraul. Eng.* **127(11)**, pp. 937–948

- DALLIMORE, C.J., HODGES, B.R. & IMBERGER, J 2003. Coupling an underflow model to a 3D hydrodynamic model. *J. Hydraul. Eng.* **129(10)**, pp. 748–757
- DAVEY, M.K., HSIEH, W.W. & WAJSOWICZ, R.C 1983. The free Kelvin wave with lateral and vertical viscosity. *J. Phys. Oceanogr.* **13**, pp. 2182–2191
- DESILVA, I.P.D., IMBERGER, J & IVEY, G.N. 1997. Localized mixing due to a breaking internal wave ray at a sloping bed. *J. Fluid Mech.* **350**, pp. 1–27
- ELLISON, T.H. & TURNER, J.S. 1959. turbulent entrainment in stratified flows. *J. Fluid Mech.* **6**, pp. 423–448
- FARMER, D.M. 1978. Observations of long nonlinear waves in a lake. *J. Phys. Oceanogr.* **8**, pp. 63–73.
- FISCHER, H.B., LIST, E.G., KOH, R.C.Y., IMBERGER, J. & BROOKS, N.H.. 1979 *Mixing in Inland and Coastal Waters*. Academic Press.
- FOZDAR, F.M., PARKER, G.J. & IMBERGER, J 1985. Matching temperature and conductivity sensor response characteristics. *J. Phys. Oceanogr.* **15(11)**, pp. 1157–1569
- GARRETT, C. & MUNK, W. 1972. Space-time scales of internal waves. *Geophys. Fluid Dyn.* **2**, pp. 225–264.
- GILL, A.E. 1997. *Atmosphere-ocean dynamics* Academic Press.
- GLORIOSO, P.D. & DAVIES, A.M. 1995. The influence of eddy viscosity formulation, bottom topography and wind wave effects upon the circulation of a shallow bay. *J. Phys. Oceanogr.* **25**, pp. 1243–1264.
- GRIFFIES, S.M., PACANOWSKI, R.C. & HALLBERG, R.W 2000. Spurious diapycnal mixing associated with advection in a z-coordinate ocean model. *Mon. Weather Rev.* **128**, pp. 538–564
- GROSS, E.S., CASULLI, V., BONAVENTURA, L. & KOSEFF, J.R. 1998. A semi-implicit method for vertical transport in multi-dimensional models. *Numer. Methods Fluids* **28**, pp. 157–186
- HEAPS, N.S. & RAMSBOTTOM, A.E. 1966. Wind effects on the water in a narrow two-layered lake. *Philas. Trans. R. Soc. London, Ser. A.* **259**, pp. 391–430.
- HENDERSON-SELLERS. B. 1966. Calculating the surface energy balance for lake and reservoir modelling: a review. *Reviews of Geophysics* **24(3)**, pp. 625–649.
- HICKS, B.B.. 1975 A procedure for the formulation of bulk transfer coefficients over water. 8:315-324. *Boundary Layer Meteorology* **8**, pp. 315–324.
- HODGES, B.R. 1997. *Numerical Techniques in CWR-ELCOM* CWR ED Number WP 1422BH.

- HODGES, B.R. & STREET, R.L. 1999. On simulation of turbulent nonlinear free-surface flows. *J. of Comp. Phys.* **151**, pp. 425–457.
- HODGES, B.R., IMBERGER, J., SAGGIO, A. & WINTERS, K.B. 2000 Modeling basin-scale internal waves in a stratified lake. *Limnol. Oceanogr.* **45**, pp. 1603–1620.
- HOPFINGER, E.J. 1987. Turbulence in stratified fluids: A review. *J. Geophys. Res.* **92**, pp. 5287–5303.
- HORN, D.A., IMBERGER, J. & IVEY, G.N. 1999. Internal solitary waves in lakes - a closure problem for hydrostatic models. *Proceedings of Aha Halikoa Hawaiian Winter Workshop, January 19 - 22* University of Hawaii, Manoa
- HSIEH, W.W., DAVEY, M.K. & WAJSOWICZ, R.C. 1983. A semi-implicit method for vertical transport in multi-dimensional models. *J. Phys. Oceanogr.* **13**, pp. 1383–1397
- IMBERGER, J. 1994. Transport processes in lakes: A review *Limnology now: A paradigm of planetary problems: R. Margalef (ed.)*. Elsevier Science, pp. 79–193
- IMBERGER, J., BERMAN, T., CHRISTIAN, R.R., SHERR, E.B., WHITNEY, D.E., POMEROY, L.R., WEIGERT, R.G. & WIEBE, W.J. 1983. The influence of water motion on the distribution and transport of materials in a salt marsh estuary. *Limnol. Oceanogr.* **28**, pp. 201–204
- IMBERGER, J. & IVEY, G.N. 1991. On the nature of turbulence in a stratified fluid, part 2: Application to lakes. *J. Phys. Oceanogr.* **21**, pp. 659–680
- IMBERGER, J. & PATTERSON, J.C. 1981. A dynamic reservoir simulation model - DYRESM 5. *Transport models for inland and coastal waters H. Fischer (ed.)*. Academic Press., pp. 310–361
- IMBERGER, J. & PATTERSON, J.C. 1981. Physical limnology. *Adv. Appl. Mech.* **27**, pp. 303–475
- ISERLES, A. 1996. Biorthogonal polynomials: Recent developments. *Numerical Algorithms.* **11**, pp. 215–228
- IVEY, G.N. & IMBERGER, J. 1991. On the nature of turbulence in a stratified fluid, part 1: The energetics of mixing. *J. Phys. Oceanogr.* **21**, pp. 650–658
- IVEY, G. & NOKES, R.I. 1989. Vertical mixing due to the breaking of critical internal waves on sloping boundaries. *J. Fluid Mech.* **204**, pp. 479–500
- JACQUET, J. 1983. Simulation of the thermal regime of rivers. *Mathematical modeling of water quality: Streams, lakes and reservoirs: G.T. Orlob (ed.)*. Wiley-Interscience
- KALIKHMAN, I., WALLINE, P. & GOPHEN, M. 1992. Simultaneous patterns of temperature, oxygen, zooplankton and fish distribution in Lake Kinneret, Israel. *Freshwater Biol.* **28**, pp. 337–347

- KOTSOVINOS, N.E. & LIST, E.J. 1975. Plane turbulent buoyant jets. Part I. Integral properties. *J. Fluid Mech.* **81**, pp. 25–41
- KOWALIK, Z. & MURTY, T.S. 1993. *Numerical modeling of ocean dynamics*. World Scientific.
- KRAUS, E.B. & TURNER, J.S. 1967. A one-dimensional model of the seasonal thermocline: II. The general theory and its consequences. *Tellus* **19**, pp. 98–106
- LAVAL, B.E., HODGES, B.R. & IMBERGER, J. 2003. Numerical Diffusion in 3D, Hydrostatic, Z-Level, Lake Models. *J. Hydraul. Eng.* **129(3)**, pp. 215–224
- LAVAL, B.E. & IMBERGER, J. 1998. Turbulent benthic boundary layer mixing events in fresh water lakes. *Physical processes in lakes and ocean. Coastal and Estuarine Studies, V. 54 J. Imberger (ed.), American Geophysical Union.* **129(3)**, pp. 503–516
- LEONARD, B.P. 1991. The ULTIMATE conservative difference scheme applied to unsteady onedimensional advection *Comp. Meth. in Applied Mech. and Eng.* **88**, pp. 17–74
- LIN, B. & FALCONER, R.A. 199y. Tidal Flow and Transport Modeling Using ULTIMATE QUICKEST Scheme. *J. Hydraul. Eng.* **123(4)**, pp. 303–314
- MARTIN, P.J. 1985. Simulation of the mixed layer at OWS November and Papa with several models. *J. Geophys. Res.* **90**, pp. 903–916
- MCCORMICK, M.J. & MEADOWS, G.A. 1988. An intercomparison of four mixed layer models in a shallow inland sea. *J. Geophys. Res.* **93**, pp. 6774–6788
- MELLOR, G.L. & YAMADA, T. 1982. Development of a turbulence closure model for geophysical fluid problems. *Rev. Geophys. Space Phys.* **20**, pp. 851–875
- MICHALLET, H. & IVEY, G.N. 1999. Experiments on mixing due to internal solitary waves breaking on uniform slopes. *J. Geophys. Res.* **104**, pp. 13476–13477
- MONISMITH, S.G. & FONG, D.A. 1996. A simple model of mixing in stratified tidal flows. *J. Geophys. Res.* **101**, pp. 28583–28595
- MORTIMER 1974. Lake hydrodynamics.. *Mitt. Int. Ver. Limnol.* **20**, pp. 124–197
- OSTROVSKY, I., YACOBI, Y.Z., WALLINE, P. & KALIKHMAN, W.J. 1996. Seiche-induced mixing: Its impact on lake productivity. *Limnol. Oceanogr.* **41**, pp. 323–332

- OU, H.W. & BENNET, J.R. 1979. A theory of mean flow driven by long internal waves in a rotating basin with application to Lake Kinneret. *J. Phys. Oceanogr.* **9**, pp. 1112–1125
- PAN, H., AVISSAR, R. & HAIDVOGEL, D.B. 1996. Three-dimensional numerical modelling of summer water motions and temperature structure in Lake Kinneret. *Eos Trans. 79 Ocean Sciences Meeting Supplement, OS120-7*.
- PHILLIPS, O.M. 1977. *A simple model of mixing in stratified tidal flows*. Cambridge University Press.
- RODI, R.D. 1987. Examples of calculation methods for flow and mixing in stratified flow. *J. Geophys. Res.* **92**, pp. 5305–5328
- ROE, P.L. 1981. Approximate Riemann solvers, parameter vectors, and difference schemes *J. Computat. Phys.* **43**, pp. 357–372
- ROMEA, R.D. & ALLEN, J.S. 1984. The effect of friction and topography on coastal internal Kelvin waves at low latitudes. *Tellus*. **36A**, pp. 384–400
- SAGGIO, A. & IMBERGER, J. 1998. Internal wave weather in a stratified lake. *Limnol. Oceanogr. Limnol. Oceanogr.* **43**, pp. 1780–1795
- SERRUYA, S. 1975. Wind, water temperature and motions in Lake Kinneret: General pattern. *Verh. Int. Ver. Limnol.* **19**, pp. 73–87
- SMOLARKIEWICZ, P.K. & PUDYKIEWICZ, J.A. 1992. A class of semi-Lagrangian approximations for fluids. *J. Atmos. Sci.* **49**, pp. 2082–2096
- SPIGEL, R.H. & IMBERGER, J. 1980. The classification of mixed-layer dynamics in lakes of small to medium size. *J. Phys. Oceanogr.* **10**, pp. 1104–1121
- SPIGEL, R.H., IMBERGER, J. & RAYNER, K.N. 1986. Modeling the diurnal mixed layer. *Limnol. Oceanogr.* **31**, pp. 533–556
- STANFORTH, A. & COTE, J. 1991. Semi-Lagrangian Integration Schemes for Atmospheric Models A Review. *Monthly Weather Review.* **119(9)**, pp. 2206–2223
- STERL, A. & KATTENBERG, A. 1994. Embedding a mixed layer model into an ocean general circulation model of the Atlantic: The importance of surface mixing for heat flux and temperature. *J. Geophys. Res.* **99**, pp. 14139–14157
- SWINBANK, W. C. 1963. Longwave radiation from clear skies. *Quarterly Journal of the Royal Meteorological Society.* **89**, pp. 339–348

- TENNESSEE VALLEY AUTHORITY 1972. Heat and mass transfer between a water surface and the atmosphere *Water Resources Research Laboratory Report 14, Report No. 0-6803*.
- THORPE, S. 1998. Some dynamical effects of the sloping sides of lakes.. *Physical processes in lakes and oceans. Coastal and Estuarine Studies V. 54 J. Imberger (ed.) American Geo-physical Union*.
- UNESCO 1981. *Technical papers in Marine Science. No. 36*
- WALLACE, J.M. & HOBBS, P.V. 1977. Atmospheric Science: an introductory survey. *Academic Press*
- WINTERS, K.B., LOMBARD, P.N., RILEY, J.J. & D'ASARO, E. 1995. Modeling the diurnal mixed layer. *J. Fluid Mech.* **289**, pp. 115–128